

This is the preprint version of the contribution published as:

Vehmas, T., **Montoya, V.**, Alonso, M.C., Vašíček, R., Rastrick, E., Gaboreau, S., Večerník, P., Leivo, M., Holt, E., Fink, N., Mouheb, N.A., Svoboda, J., Read, D., Červinka, R., Vasconcelos, R., Corkhill, C. (2020):

Characterization of Cebama low-pH reference concrete and assessment of its alteration with representative waters in radioactive waste repositories

Appl. Geochem. **121** , art. 104703

The publisher's version is available at:

<http://dx.doi.org/10.1016/j.apgeochem.2020.104703>

41 expected, the size of the pores in the hydrated cement phases varies from the micro- to the nanoscale.
42 Connected porosity of both materials were low. Compressive strength of the concrete was 115 MPa,
43 corresponding to traditional high-performance concrete. Degradation of these materials in contact with
44 different waters mainly produce their decalcification and enrichment in Mg for waters containing high
45 amount of this element, like the clay waters.

46

47 **KEYWORDS:** Low-pH cement, Blast furnace slag, Nuclear Waste Repository, Concrete, Mortar

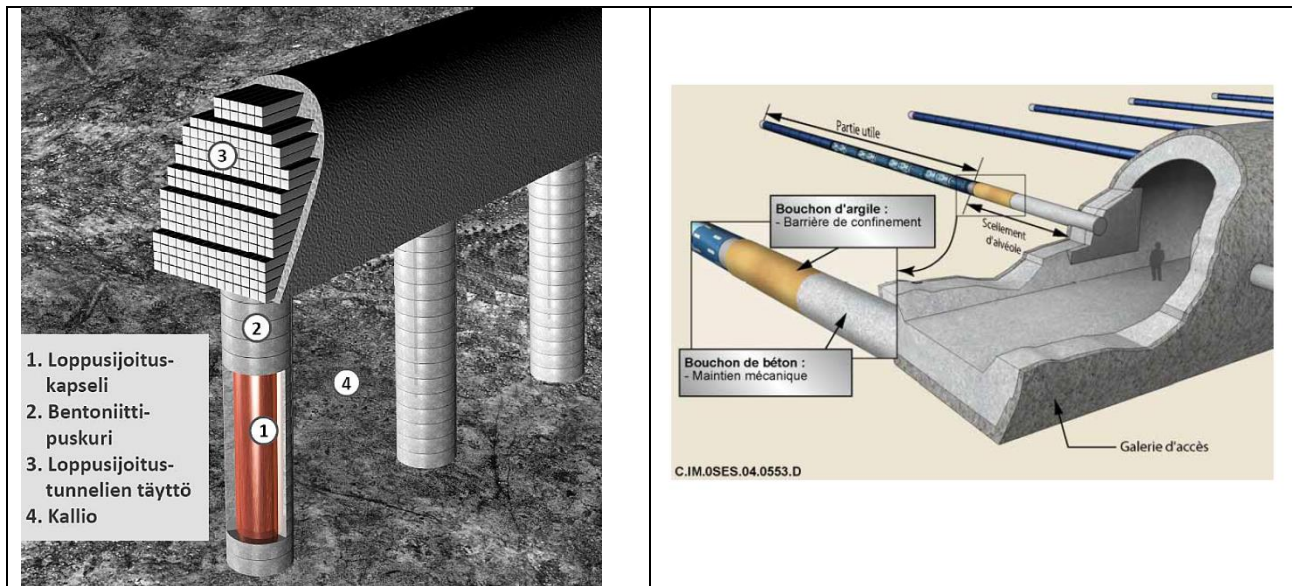
48

49 **1. INTRODUCTION**

50 Nuclear power generation is a viable solution for decreasing CO₂ emissions and mitigating climate change at
51 an intermediate time scale. However, a major disadvantage is production of nuclear waste in various forms
52 and levels of radioactivity. The management and disposal of high-level waste (HLW) consisting of chemically
53 processed and vitrified spent nuclear fuel or spent fuel itself will become a major task. Although the volume
54 of HLW is small, compared to the total volume of nuclear waste generated, it contains 95% of the total
55 radioactive inventory (World Nuclear Association, 2019).

56 Deep underground repositories are the most likely option for final disposal of HLW as well as for the
57 Intermediate Level Long Lived Waste (IL-LLW). Depending on the selected site, final disposal concepts will
58 vary to suit local conditions. However, all concepts must assure their long-term safety for periods ranging
59 from tens of thousands to a million year, minimizing the release of radionuclides into the environment.
60 According to current plans, the first HLW operational repositories will be in the Nordic countries and
61 emplaced in crystalline bedrock (Posiva Oy, 2020). Clay-rock repositories are also a widely studied option,
62 which will shortly follow crystalline-rock repositories (Nagra, 2019).

63 In deep underground repositories, HLW is disposed of in bedrock hundreds of metres below the surface,
64 which naturally isolates the waste from the biosphere. The safety of the repository is ensured via a
65 combination of natural and engineered barriers (see Figure 1). In the case of the KBS-3 disposal concept in
66 crystalline rock (Moren, 2010), the engineered and geological barrier system comprises water- and gas-tight
67 sealed copper canisters with a cast iron insert and the bentonite-based buffer, the backfill materials
68 (Palomäki and Ristimäki, 2013) and the surrounding bedrock. Bentonite has an important role in many
69 repository concepts, protecting the canister from small bedrock movements and potentially adsorbing any
70 radionuclides released from the primary containment. Additionally, bentonite inhibits groundwater
71 penetration into the repository and is intended to return the disposal environment to one close to natural
72 conditions due to wetting-induced swelling (Palomäki and Ristimäki, 2013), Koskinen, 2014). On the other
73 hand, concrete and other cementitious materials are used significantly in repositories for structural support
74 and isolation purposes but also as engineered barrier, depending on the concept. For example, concrete
75 plugs are used for sealing the repository and the deposition tunnels whilst also ensuring mechanical and
76 hydrological isolation of various repository compartments (see Figure 1). In addition to concrete plugs,
77 cementitious materials are used in shotcrete for tunnel wall rock supports, rock-bolting grouts and injection
78 grouts for fissure sealing. However, independently, of their function, it is important that cementitious
79 materials do not alter the engineered barrier system's performance within the long lifetime of the repository
80 in order to meet safety requirements.



81 **Figure 1.** Left: multi-barrier system used in the KBS-3 concept. 1) Copper Canister, 2) Bentonite buffer 3)
 82 Bentonite backfill material 4) Bedrock (crystalline rock). Photo from the courtesy of Posiva Oy. Right: C-type
 83 waste (HLW) disposal cells of ANDRA (France), extracted from Dossier 2005 (ANDRA 2005).

84 As indicated in Figure 1, groundwater or porewater, backfill/buffer and closure materials can be in direct
 85 contact with cementitious materials. Due to their different chemical properties, interactions between them
 86 will occur at the interfaces. These interactions could potentially involve changes in key properties of the
 87 buffer and host rock such as, geochemical composition, swelling pressure, hydraulic conductivity and pore
 88 structure. Migration of cementitious leachates may also affect the bentonite buffer, despite not being in
 89 direct contact with cementitious materials (Koskinen, 2014). For this reason, cementitious mix designs having
 90 suitable composition with respect to bentonite stability have been formulated (Bach, 2010; Cau Dit Coumes
 91 et al., 2006; Codina et al., 2008; Dole and Mattus, 2007; Garcia Calvo et al., 2010; Garcia et al., 2007; Holt et
 92 al., 2014; Lothenbach et al. 2008; Martino, 2007; Nishiuchi et al., 2007). These “low-pH” formulations consist
 93 of low alkaline Portland cements mixed with large amounts of supplementary pozzolanic materials (i.e silica
 94 fume or fly ash) and hydraulic materials (i.e. blast furnace slag), which hydrate themselves or react with the
 95 hydration products that control the pH and composition of cement pore solution. Consequently, these mix
 96 designs are still highly basic but the pH value is significantly lower than in traditional Portland cements.
 97 Mechanical properties and durability are usually considered to be similar to ordinary Portland cement-based
 98 formulations, although some disagreements still remain in terms of mechanical resistance against different
 99 waters attack (Dauzères et al., 2014).

100 Good examples of “low-pH” formulations are the successful casting and demonstration of massive tunnel
 101 end plugs, drifts and seals with ternary blended cements described in the DOPAS project (Holt et al., 2016),
 102 Noiret et al., 2012). In this case, the “low-pH” concrete consisted of a ternary blend with low-alkali ordinary
 103 Portland cement, granulated silica fume and low-calcium fly ash. Although fly ash has been demonstrated to
 104 be a good option for “low-pH” mix designs (i.e. low water demand, relatively inexpensive material, high
 105 amorphous content), it also has drawbacks. For example, fly ash is a by-product of energy generation from
 106 combustion of fossil coal. As combustion of fossil coal is likely to be reduced over the next years, fly ash might
 107 not remain available throughout the construction and operational periods of a repository. Even if fly ash
 108 remains available throughout the repository construction period, it is expected that quality may decrease
 109 owing to the use of alternative fuel resources. The inhomogeneity of fly ash is already a problem, which will
 110 likely increase in the future (Taylor, 1997).

111 For the above reasons, new concrete designs are formulated and tested in order to fulfil the needed

112 requirements to be used in nuclear waste disposal. Slag-based “low-pH” mix designs has also recently shown
 113 to have multiple benefits (Lothenbach et al., 2008, 2012a). Blast furnace slag is an industrial by-product of
 114 iron and steel production with the advantage that it has substantially greater homogeneity than fly ash due
 115 to production requirements. Due to the nature of its production, blast furnace slag is likely available
 116 throughout the anticipated repository construction period. It is also a source of calcium but without the
 117 excessive heat of traditional Portland cement, limiting temperature development in massive structures.

118 In this work a new reference concrete and micro-mortar slag-based ternary mixes were designed and
 119 characterized as potential material to be used in the context of nuclear waste disposal, which require high
 120 durability during the extremely long times of disposal. Mechanical, chemical, microstructural and hydraulic
 121 characterization were performed by eight laboratories of the Cebama (Cement-based materials, properties,
 122 evolution, barrier functions) project consortium. The basis of the Cebama reference concrete was a ternary
 123 mix design that has been used successfully in full scale demonstrations (Holt and Koho, 2016; Leivo et al.,
 124 2014). The micro-mortar version was used to provide more detailed information on the binder phase and
 125 can be considered as an aggregate-free concrete.

126 In addition, alteration and evolution with time of the designed concrete and micro-mortar in contact with
 127 different representative waters in radioactive waste repositories (i.e. clay, crystalline, saline, bentonite) have
 128 been studied by percolation, compressive punch test and leaching experiments.

129

130 2. MATERIALS

131 2.1. Cebama reference concrete and micro-mortar

132 The mix designs for the concrete and micro-mortar are presented in Table 1. Although materials used for
 133 their design were the same (except the aggregates), it is clear that direct comparison between both materials
 134 is not possible as the ratios between the different materials and water are very different. The ordinary
 135 Portland cement (OPC) used was low-alkali, medium heat ordinary Portland cement LA MH CEM I 42.5 from
 136 CEMENTA Ab (Annläggningcement Degerhamn). Granulated silica fume (SF) and blast furnace slag (BFS) were
 137 from Finnsementti Oy (Parmix silika and Masuunikuona KJ400). Elemental compositions of the binder
 138 materials were determined by X-ray fluorescence (XRF) and are presented in Table 2. The superplasticizer for
 139 achieving the target workability was a naphthalene sulfonate (Pantarhit LK FM from Ha-Be Betonchemie
 140 GmbH. Alternatively, a similar naphthalene sulfonate superplasticizer from DEN BRAVEN Czech and Slovak a.s.,
 141 was used for some of the compressive punch strength tests (see section 3). The aggregate was a local granitic
 142 material of Finnish origin from Rudus Oy. The particle size distribution of aggregates is presented in Table 1.
 143 Quartz filler was from Sibelco Nordic Oy (Nilsjö). A description of the batching procedure and more details of
 144 the mix design and materials are available elsewhere (Vehmas et al., 2017). The major components,
 145 calcium/silica -ratio, binder content and water/binder -ratio were the same as those of the silica and fly ash
 146 based ternary blends described in the literature (Vehmas et al., 2017). Samples were cured for 24 hours at
 147 room temperature and relative humidity of 100%. After 24 hours, samples were demoulded and cured
 148 submerged in water up to an age of 28 days.

149 **Table 1.** Mix designs of studied “low-pH” concrete and micro-mortar.

Materials	Concrete [kg/m ³]	Micro-mortar [kg/m ³]
CEM I 42.5	105	468
Silica fume	110	491
Blast furnace slag	65	290
Quartz filler*	116	517

Agregates:		
0-1 mm	168	-
1-8 mm	770	-
8-16 mm	532	-
16-32mm	396	-
Water (effective)	120	312
Superplasticizer	16.8	75
Water/binder -ratio	0.43	0.25

150 ****Particle size distribution: (70% < 63 μm and 30% between 63- 250 μm)**

151 **Table 2. Oxide composition of the binder materials (wt. %)**

Binder	CaO	SiO ₂	Al ₂ O ₃	SO ₃	MgO	Fe ₂ O ₃	K ₂ O	Na ₂ O	CO ₂ ^a	TiO ₂	MnO	SrO	ZrO ₂
SF	1.46	93.1	1.44	0.47	0.88	0.91	1.73	-	<i>n.d.</i>	-	-	-	-
OPC	66.2	17.9	3.52	3.92	0.68	5.17	0.645	0.08	1.32	0.23	0.25	0.03	0.01
BFS	42.3	32.6	10.23	2.54	7.86	0.78	0.61	0.62	<i>n.d.</i>	1.70	0.38	0.05	0.03

152 *n.d.* = not determined. ^aCO₂ obtained by thermogravimetric analysis

153 2.2. Representative water compositions in Nuclear Waste Disposal

154 Different groundwater and porewater compositions have been used in the leaching, compressive strength
 155 evolution measurements and percolation experiments (see section 3). Water compositions are presented in
 156 Table 3 and detailed information on the groundwater origin and compositions are provided in the following
 157 references. In short, granitic waters (Granitic I, Granitic II and Granitic III) represent the artificial Allard
 158 (Lagerblad and Trägårdh, 1994), Grimsel (Turrero et al., 2006) and a natural water occurring in the Josef
 159 underground laboratory (Czech Republic), respectively. Saline groundwater represented an artificial NASK
 160 water (Gascoyne, 2002; Lagerblad and Trägårdh, 1994). Clay I emulated a Callovo-Oxfordian clay formation
 161 pore water (Vinsot et al., 2008), Holt et al., 2016) and Clay II a Febex bentonite porewater (Turrero et al.,
 162 2006, 2011). The B75 water was prepared by using a bentonite B75 suspension and the Granitic water III (S:L
 163 ratio 1:5) (Večerník et al. 2016). Bentonite artificial porewater was prepared inside an argon (Ar) glove-box
 164 according to the water composition provided by (Bradbury and Baeyens, 2011) for a MX-80 bentonite.

165

166 **Table 3. Groundwater and porewater composition (mg/l), used in the methods described in the section 3.**

[mg/l]	Granitic I	Granitic II	Granitic III	Saline	Clay I	Clay II	B75	Bentonite*
Na	63.2	0.4	18.3	3035.9	1118.1	130.0	349.0	5773
K	4.1	0.0	2.0	104.7	52.6	0.7	13.0	73.6
Mg	4.7	0.0	15.4	8.2	153.7	8.9	3.9	230
Ca	16.2	0.2	76.1	682.3	241.4	11.0	5.0	596
Sr	-	-	-	-	-	-	-	9.1
Al	-	-	-	-	-	-	-	0.01200
Fe	-	-	-	-	-	-	-	0.8x10 ⁻³
Cl	75.2	0.0	14.7	6246.9	1901.5	24.0	21.4	8271.5
Br	-	-	-	-	-	-	-	-
SO₄	7.4	0.1	106.2	470.1	1434.8	76.0	159.5	694.8
Si	-	-	-	-	-	-	-	2.1
HCO₃⁻	-	0.4	199.6	-	-	3.2	604.1	12.3
pH	8.1	9.7	7.7	7.6	6.3	8.0	8.8	8.0

167 *artificial porewater prepared inside an argon (Ar) glove-box according to the water composition provided by
 168 (Bradbury and Baeyens, 2011). Different amounts of solids (20.18 g NaCl, 0.23 g KCl, 3.04 g MgCl₂·6H₂O, 0.857
 169 g MgSO₄·7H₂O, 0.06 g SrCl₂·6H₂O, 0.094 g Na₂CO₃, 19.89 g Na₂SO₄, 4.11 g CaCl₂·2H₂O, 10.01 g CaCO₃) were
 170 dissolved in 2 L ultrapure water (MilliQ system, Millipore) in a PE bottle. Additionally, 60 µL of a solution of
 171 6.16 M Na₂O₇Si₃ (water glass) and 16 mL of sulfuric acid H₂SO₄ (0.04 M) were added to adjust the silicon
 172 content and the pH of the solution, respectively.

173

174 3. METHODS

175 3.1 Characterization of the micro-mortar

176 Workability was measured using the Haegermann method according to DIN 1164. Air content, compressive
 177 strength and density were determined according to standards (SFS-EN 12350-2, SFS-EN 12350-7, EN 12390-
 178 3 and EN12390-9). Additionally, the time evolution of the compressive strength was determined using a non-
 179 standard compressive punch test (Czech Geological Institute, 1987, Večerník et al., 2016, Vašiček et al. 2019)
 180 with thin cylindrical plates with high surface/ volume ratio (diameter, 50.0 mm and thickness, 8.2 mm). In
 181 short, the sample is located between two punches (diameter 7.98 mm with contact area of 50 mm²) and
 182 loaded until breakage while a force is applied (F, [N]). The press head displacement (related to deformation
 183 of the sample) is recorded. Verification of the punch method by comparison with the standard one described
 184 in ČSN EN 196-1 (using 40 mm cubes) was also performed. Various mortars with different uniaxial strength
 185 were tested by both methods to verify the relation of standard and non-standard tests. The value of uniaxial
 186 punch strength R_p [MPa] was calculated as described in (Czech Geological Institute, 1987):

187

188

189

$$R_p = F^*/A \quad (\text{Equation 1.})$$

190 where A is an ideal area (123 mm²) for punch of 7.98 mm and 50 mm diameter sample and a linear
 191 relationship was used to correlate the non-standard with the standard test results R_{cube} [MPa] (Večerník et
 192 al., 2016):

193

194

$$R_{cube} = R_p * 1.609 + 6.939 \quad (\text{Equation 2.})$$

195 Punch test were performed using various groundwater compositions (Granitic III and B75 indicated in Table
 196 3) and temperatures in order to evaluate groundwater influence on mechanical properties. The rigidity (or
 197 stiffness) [kN/mm] was derived from the linear section of force/ displacement relation of the particular
 198 strength test to have another indicator of potential changes of mechanical properties. Each punch test result
 199 consisted of 9-12 measurements according to available number of tested samples. Then the average value
 200 of each dataset was provided. Statistical evaluation (test for outliers and uncertainty calculation with
 201 confidence interval 95 %) was performed for each dataset. Expanded relative uncertainties of the sets were
 202 between 0.8 % and 8.2 % (only 3 datasets had an uncertainty above 5.3 %).

203

204 The chemical and structural properties were determined by using different complementary techniques.
 205 Initially, 5 mm of sample was removed from the surface to obtain regions unaffected by atmospheric carbon
 206 dioxide. For analysis by X-Ray Diffraction (XRD), thermogravimetric analysis / differential scanning
 207 calorimetry (TG-DSC) and ²⁹Si and ²⁷Al Magic Angle Spinning Nuclear Magnetic Resonance (²⁹Si and ²⁷Al MAS
 208 NMR), samples were crushed manually and powdered in an agate-ball grinder for only 2 minutes to avoid
 209 changes in the phase assemblage due to grinding (Scrivener et al. 2018). Ground samples were immersed in
 210 isopropanol for 15 minutes, then filtered using a Buchner funnel. The samples were dried in a compartment

211 dryer at 40°C for 10 min to ensure elimination of isopropanol. For X-ray absorption spectroscopic
212 measurements, pellets were pressed after mixing powdered samples with boron nitride.

213

214 Scanning electron microscopy - energy dispersive X-ray spectroscopy (SEM-EDX) measurements were
215 performed using an ESEM (model FEI Quanta 650 FEG), equipped with an EDX spectrometer (model Thermo
216 Scientific NORAN System 7) for elemental microanalysis. XRD analysis was performed with a Bruker D8
217 ADVANCE diffractometer using Cu K α radiation under controlled N₂ atmosphere using a low background and
218 air-tight sample holder. TG-DSC was conducted using a heating rate of 10°C/min from 25 to 1200 °C with a
219 STA409 (Netzsch Gerätebau GmbH) under N₂ atmosphere. The ²⁹Si and ²⁷Al MAS NMR spectra were acquired
220 with Bruker Avance III 400 wide-bore spectrometer with a magnetic field strength of 9.4 T at 104.28 MHz for
221 ²⁷Al and 79.50 MHz for ²⁹Si. Free induction decay was recorded with only 8k-16k data points. The observed
222 ²⁹Si resonances were analysed using the Q_n(mAl) classification (where Q refers to a Si tetrahedron connected
223 to n Si tetrahedral with n varying from 0 to 4 and m indicating the number of neighbouring AlO₄ tetrahedra.
224 (Engelhardt and Michel, 1987)

225 Additional information about the mineralogical composition was provided by X-ray absorption spectroscopy
226 (XAS) at the Fe and Cl K-edges. XAS is complementary to the above mentioned techniques, it is element
227 specific and does not suffer from overlapping signals from Al- and Fe-containing phases. Furthermore, the
228 application of XAS does not require compounds to be crystalline. Fe K-edge XAS data were recorded at the
229 BM26A beamline (Nikitenko et al., 2008) at the European Synchrotron Radiation Facility (ESRF, Grenoble,
230 France). Fe K-edge spectra for powdered micro-mortar, concrete and reference compounds were recorded
231 either in transmission or in fluorescence detection mode using a 9 element monolithic Ge fluorescence
232 detector. Selected reference compounds are C2F (Ca₂Fe₂O₅), C4AF (Ca₂FeAlO₅), the starting clinker (LA MH
233 CEM I 42.5 from Cementa Ab), hematite (α -Fe₂O₃), ferrihydrite, silica fume (Elkem, USA) (see Table 2 for iron
234 content), C-S-H phases and ferric sulphate (Fe₂(SO₄)₃.xH₂O), Alfa Aesar). The Fe K-edge spectrum of goethite
235 was recorded in transmission mode at the BM30 beamline (Proux et al., 2006) at the ESRF. At all stations, the
236 energy of the incoming X-ray beam was calibrated by assigning the first inflection point of the transmission
237 Fe K-edge X-ray absorption near-edge structure (XANES) recorded for a Fe foil to 7112.0 eV. Cl K-edge XAS
238 data were recorded at the INE-Beamline (Rothe et al., 2012) at the KIT Synchrotron Light Source (Karlsruhe,
239 Germany) in fluorescence detection mode using a silicon drift detector. At this edge, the energy of the
240 incoming X-ray beam was calibrated by assigning the maximum of the absorption edge recorded for KCl to
241 2822.8 eV. Several chlorine reference compounds were used, and solid compounds were stored in an oven
242 at 40°C for at least 12 hours before measurements. Solutions were also prepared: 0.5 mol/l NaCl and an
243 artificial cement porewater or ACW (5.9 mmol/l Na⁺, 3.8 mmol/l K⁺, 3.6 mmol/l Ca²⁺, 2.8 μ mol/l CO₃²⁻, 5.8
244 mmol/l SO₄²⁻ and 3.8 mmol/l Cl⁻, pH = 11). XAS data were treated following standard procedures using the
245 Athena interface to the Iffeffit software (Ravel and Newville, 2005).

246 The evolution of the hydration process was monitored via pH and chemical composition analysis as a function
247 of hydration time. For the analysis of pore water pH and chemical composition, the *ex-situ* leaching method
248 described by (Alonso et al., 2012) was used. This method consists on mixing a certain amount of cement
249 powder with deionised CO₂-free water obtaining a liquid/solid ratio equals to 2.5 L kg⁻¹. After an equilibration
250 time of two weeks, phase separation is achieved by centrifuging the samples. Then, the supernatant from
251 each container is filtrated and the composition and pH is analysed.

252 3.2 Leaching studies with the micro-mortar

253 Leaching studies of micro-mortar with different waters were performed at room temperature (20°C) by using
254 two slightly different set-ups. The age of the micro-mortar in these studies were more than 5 months. In the
255 experimental set-up used to study the alteration of the micro-mortar with the Clay I (Callovo Oxfordian),
256 Crystalline I and Saline -groundwaters (see Table 3), the micro-mortar sample was submerged in the solution
257 at a solid/liquid ratio of 1 at the age of 28 days. 200 cm³ micro-mortar cylindrical blocks (dimensions: 6.6 cm
258 diameter and 5.9 cm height) were submerged in 200 cm³ synthetic water and not changed throughout the

259 experiment. The pH of the aqueous phase was determined using a Thermo Fisher Scientific Orion™
260 9165BNWP Combination Sure-Flow pH electrode, calibrated to pH 10.01 and 13.00 with standard buffer
261 solutions. The experiments were performed in triplicate. The alteration zone was characterised SEM-EDX.
262 The experimental set-up used to study the alteration of the micro-mortar with bentonite water was
263 performed to fully saturated samples. Cubic samples (10x 10 x 10 mm) were sealed with an epoxy resin,
264 except for the exposed surface. The samples were submerged in 40 ml bentonite porewater (Table 3) for 6
265 months in a controlled argon atmosphere. After exposure, the micro-mortar samples were immersed in
266 isopropanol to displace the water and stop further reactions. The alteration zone was characterised by
267 cutting the sample parallel to the flow direction and identifying the chemical perturbation using SEM-EDX.
268 Additionally, after 6 months, the bentonite water was analysed for its concentration of cations and anions by
269 inductively coupled plasma optical emission spectrometry (ICP-OES), inductively coupled plasma mass
270 spectrometry (ICP-MS) and ion chromatography (IC).

271 Finally leaching experiments at different temperatures (10°C and 95°C) with the Granitic III and bentonite
272 B75 water were performed (Vašiček et al., 2019). Micro-mortar samples were sealed in plastic tubes and the
273 pH evolution were measured according to the method described by (Alonso et al., 2012). Similarly, to the
274 previous described experiments, the alteration zone was characterised SEM-EDX

275 *3.3 Characterization of the concrete*

276 Slump, air content, compressive strength and density were measured according to standards (SFS-EN 12350-
277 2, SFS-EN 12350-7, EN 12390-3 and EN12390-9).

278 The chemical composition and structural properties were determined after 5 and 15 months aging in a
279 chamber at 100% RH and 20°C. The samples were prepared for characterisation immediately after removing
280 from the curing chamber. XRD (Bruker XD8 advance X-ray diffractometer Cu radiation), thermogravimetry
281 (STD Q600 V20.9 build 20, at a heating rate of 10°C/min)/ differential thermal analysis (TG/DTA) and SEM-
282 EDX (in polished samples, Hitachi S-4800 and Bruker 5030 EDX) were performed. XRD samples were
283 completed on enriched powder samples in cement paste by removing the coarse aggregates. Firstly the
284 coarse aggregates were removed, then the sample was drilled to smaller size and aggregates above 2 mm
285 were removed in order to enrich the sample in cement paste; finally the samples were milled up to powder
286 with particle sizes <80µm. For the SEM tests, polished samples were prepared after embedding in epoxy resin
287 and coating with carbon for characterisation. In addition, information on iron and chlorine speciation was
288 obtained in the same way described in section 3.1 for the micro-mortar and by probing their K-edge by XAS.
289 Porosity was measured using the techniques described in section 3.5.

290 Pore solution pH and composition were determined according to Alonso et al., (2012). A piece of concrete
291 was powder grounded without removing the aggregates, to a particle size of 80 µm. 10g were mixed with
292 10mL of deionised water. The suspension stirred for 5 min and then filtered with 0.45µm filter. The pH was
293 measured with a pH electrode stable in the alkaline range of 12. The ion content was determined by ionic
294 chromatography without any dilution or acidification of the system.

295

296 *3.4 Percolation experiments with the concrete*

297 The experimental set-up described in Garcia-Calvo et al. (2010) was used for the percolation experiments. A
298 concrete slice of 5 cm diameter and 5 cm length was placed between two cylinders of methacrylate of the
299 same diameter. These cylinders of methacrylate contain holes in the centre which are used for the entry and
300 exit of the injected water. The set of methacrylate and concrete was inserted in a rubber tube and this in
301 turn in a methacrylate tube of about 15 cm of height and radius similar to the cylinders and the sample. The

302 possible gaps between the methacrylate tube and the rubber were sealed with epoxy resin to ensure that
 303 water circulated only through the pore network of the concrete sample. A constant water pressure of 8 MPa,
 304 was maintained to percolate groundwaters through the concrete samples of 5x5cm. The age of the samples
 305 at the initial of percolation tests was 5 months. The percolated water composition and pH were monitored
 306 during the test, including the volume of the effluent flux to obtain the hydraulic conductivity. Additionally, at
 307 the end of each percolation test, the chemical, mineralogical and microstructural alterations in concrete were
 308 analysed at several distances from the groundwater inlet using XRD, TG/DTA and SEM.

309

310 *3.5 Porosity and density measurements (concrete and micro-mortar)*

311 Free water needs to be removed from cementitious binders prior to pore structure characterization. In the
 312 literature, different drying procedures were described to remove the free water, all of them having, in more
 313 or less extend, effects on the initial pore structure and phase evolution (Gallé, 2001; Zhang et al., 2019). For,
 314 this reason, prior to the mercury intrusion and kerosene porosimetry measurements, the concrete and the
 315 micro-mortar were heated under vacuum at 100°C for at least 36 hours and cooled under vacuum to ensure
 316 that all water left the pores, keeping in mind that this could slightly affect the studied materials.

317 Mercury intrusion porosimetry (MIP) - Intrusion and extrusion curves were obtained using Micromeritics
 318 Autopore IV 9500 volumetric set up on blocks of 2 cm³ from atmospheric pressure up to 200x10⁶ Pa.
 319 Cumulative pore throat size distribution, up to the critical pore diameter, was calculated from the intrusion
 320 curve based on Washburn's law and a contact angle of 141.3° (Washburn, 1921) , assuming a cylindrical pore
 321 shape.

322 The bulk density or apparent dry density (ρ) of each sample was obtained before the first pressure step (3x10³
 323 Pa). The total intrusion porosity φ (MIP) or connected/accessible porosity was also estimated from the
 324 maximum intruded specific volume of mercury V (intr.max) [m³/kg] and ρ , [kg/m³] using the following
 325 Equation 3.

$$326 \quad \varphi(\text{MIP}) = V(\text{intr.max}) \times \rho \quad (\text{Equation 3.})$$

327 Kerosene porosimetry - Total bulk porosity (connected (accessible) and not connected) and the apparent dry
 328 density were measured by the kerosene porosity method described in Gaboreau et al., (2011), which is based
 329 on the Archimedes' principle.

330 Calculated porosity- Porosity was also calculated from the measured grain density (ρ_{gr}) (helium pycnometry
 331 using a micromeritics accupyc 2020) and the apparent dry density (ρ) (obtained by mercury intrusion
 332 porosimetry) according to the following Equation 4.

$$333 \quad \varphi = 1 - (\rho/\rho_{gr}) \quad (\text{Equation 4.})$$

334

335 **4. RESULTS AND DISCUSSION**

336 *4.1 Fresh-stage properties*

337

338 Fresh stage properties of the concrete and the micro-mortar were measured after batching. The slump of
 339 the concrete was 180 mm, corresponding to typical easily workable concrete. The Haegermann flow of the
 340 micro-mortar was 200 mm, indicating easy-to-use mortar without risk of segregation. The fresh density of
 341 the concrete was 2420 kg/m³ and 2110 kg/m³ for the micro-mortar. The measured air content for the
 342 concrete was 1.0%.

343

344 *4.2 Mechanical properties*

345

346 The compressive strength evolution of concrete and micro-mortar are presented in Table 4 by using both
 347 standard and non-standard punch test. At the age of 7 days, the compressive strength of the concrete was
 348 47 MPa and 64 MPa for the micro-mortar. The compressive strength of the concrete was similar to high
 349 performance concrete yet the result for micro-mortar was higher than that of the concrete studied. The
 350 results on SFS-EN concrete (Table 4) show continuing, significant increase in strength between 424 and 728
 351 days (of about 30 %). This continuous evolution of the mechanical properties over 728 days (~2 years)
 352 highlight the low kinetics of hydration of the studied materials and the impossibility to reach final properties
 353 within only 28 days. The study on the interaction of micro-mortar thin samples (Table 4, referred to punch
 354 test) under various conditions (granitic/ humid air, B75 water and temperature 10 or 95 °C) shows significant
 355 hardening during the initial phase of 9 months, with indication of stabilisation during a further 9 months. The
 356 non-standard punch test method, applied only to the micro-mortar and performed at 10°C, presented similar
 357 compressive strength values to the one measured with the standard method. In addition, the use of different
 358 waters did not have a big influence in the test results. Only, the bentonitic water (B75) slightly affected the
 359 rigidity (force-deformation, [kN/mm]) (Table 5). Bentonite suspension stabilised the rigidity value slightly
 360 below the level of initial tests while the reference and non-bentonite environment allowed a slow increase
 361 of rigidity during the testing period.

362 On the other hand the compressive strength of the micro-mortar was clearly dependent on the
 363 superplasticizer used (Table 5). Keeping in mind that all the superplasticizers used in this work were
 364 naphthalene based superplasticizers. The superplasticizer had a central role in dispersing cement and
 365 supplementary cementitious materials to ensure good reactivity. High dispersion of fines also increased
 366 workability and enabled good consolidation during sample manufacture. As observed in Table 5, a change in
 367 superplasticizer brand reduced compressive strength, and even a change in the plasticizer batch had also an
 368 effect on the micro-mortar compressive strength. There is no clear explanation for this effect, especially
 369 when only the different batch of the same superplasticiser was used. Some effect could be related to the
 370 time and storage conditions of the superplasticisers before use or minor time variations in preparation
 371 procedure and varying amount of mortar in the batches. At least two series of tests were performed for each
 372 punch test and the results show the same systematic results confirming this was not an error in the
 373 measurement. Therefore, even a small change in superplasticizer quality induced changes in compressive
 374 strength. Moreover, the plasticizer dosages used in this work greatly exceeded the manufacturer's
 375 recommendations, which likely caused or increased the effects observed

376

377 **Table 4.** *Compressive strength and densities of the concrete and the micro-mortar.*

Sample:	Concrete		Micro-mortar						
Method:	SFS-EN		SFS-EN		Punch test				
Environment:	20°C RH100%		20°C RH100%		Humid air, 10°C	Granitic III, 10°C	B75, 10°C	Granitic III, 95°C	B75, 95°C
Age [d]	Compressive strength [MPa]	Density [kg/m³]	Compressive strength [MPa]	Density [kg/m³]	Compressive strength [MPa]				
7	47	2420	64	2110	-	-	-	-	-
14	-	-	-	-	67	-	-	-	-
28	80	2430	104	2150	76	-	-	-	-
64	-	-	-	-	82	-	-	-	-
275	-	-	-	-	113	132	122	146	132

424	89	2420	-	-	-	-	-	-	-
550	-	-	-	-	112	116	109	146	129
723	-	-	149	2140	-	-	-	-	-
728	116	2450	-	-	-	-	-	-	-

378

379 **Table 5.** Rigidity values obtained with the punch test

	Punch test				
	Humid air, 10°C	Granitic III, 10°C	B75, 10°C	Granitic III, 95°C	B75, 95°C
Age [d]	Rigidity [kN/mm]				
0	-	31 ± 1	-	-	-
275	35 ± 1	32 ± 1	28 ± 3	33 ± 2	26 ± 4
550	40 ± 4	38 ± 2	28 ± 6	36 ± 4	30 ± 12

380

381 **Table 6.** The effect of superplasticizer quality to compressive strength in punch test

	Punch test		
	Naphthalene (Pantarhit)	Naphthalene (Pantarhit) Different batch	Naphtalene (DEN BRAVEN)
Age [d]	Compressive strength [MPa]		
7	-	59	38
14	75	67	48
28	86	76	63
42	92	-	70
49	101	83	-
56	-	-	78
63	103	81	75

382

383 **4.3 Microstructure, petrophysical properties (porosity and density)**

384 Microstructural characterisation by SEM indicated dense C-S-H phases and low permeability structure for
385 both the concrete and micro-mortar samples. Additionally, a good aggregate-cement paste of interfacial
386 transition zone (ITZ) for the concrete was observed. Non-reacted silica fume (with a characteristic spherical
387 shape), quartz and feldspar were also observed with the same technique.

388 Total and connected porosity was determined by applying the kerosene and mercury intrusion porosimetry
389 methods, respectively (Table 7). In addition, porosity was calculated by using the grain density obtained by a
390 helium pycnometer. Calculated porosities were 24.3 and 12.8 % for the micro-mortar and the concrete,
391 respectively in agreement with the measured total porosity by the kerosene method. However, mercury
392 intrusion porosity for both, the micro-mortar and the concrete was much lower, 6.1%, and between 2.3-
393 2.5%, respectively (Table 7). This means that most of the connected pores (connected porosity) in both
394 materials have pore-throat sizes below 7nm because mercury cannot penetrate these small pore-throats [v].
395 Indeed, the mean pore size measured with mercury intrusion porosimetry was < 15 nm (Leroy et al. 2019)
396 indicating that most of the connected porosity available for transport was nano-size, and the structure of
397 concrete and micro- mortar was dense. Although some small changes could occur during the drying process
398 of the samples, prior to the porosity measurement, the general observations are still valid (Zhang et al., 2019).

399 **Table 7.** Porosities of the concrete and the micro-mortar.

Material	MIP		He pycno.	Kerosene porosity		Calculated porosity
	Bulk density (ρ) (g/cm³)	Porosity, φ_{MIP} , (%)		Bulk density (ρ) (g/cm³)	Porosity, φ_{KEP} (%)	
Micro-mortar	1.88	6.1	2.48	1.83	26.2	24.3
Concrete	2.28	2.3*-2,5**	2.61	2.28	12.5	12.8

400 *measured after 5 months ** measured after 15 months.

401

402 4.4 Chemical properties

403 Pore solution pH evolution for concrete and micro-mortar decreased over time due to proceeding pozzolanic
 404 reaction and C-S-H polymerization (see Table 8). The decrease of the Ca:Si ratio of the C-S-H phases has a
 405 large impact on the observed pH decrease in agreement with thermodynamic calculations (Idiart et al., 2020).
 406 For both materials, the pH is below than a portlandite saturated solution (pH 12.5) indicating that portlandite
 407 is not present in the system in accordance with the chemical composition expected regarding the mix
 408 formulation.

409 Elemental composition of concrete pore solution evolution with time was also determined and it is presented
 410 in Table 9. As can be observed, Al concentration decreases to very low concentrations ($\sim 4 \times 10^{-7}$ mol/l) due to
 411 the precipitation of Al- bearing phases (C-A-S-H and ettringite) which have been observed in the
 412 characterization of the solid. The same was observed for iron, in that case the precipitation of Fe-bearing
 413 phases restricted the iron concentrations to values below $< 2 \times 10^{-6}$ mol/l. Silicon concentrations in the
 414 aqueous solution remained at 1×10^{-3} mol/l and calcium concentration decreased slightly with time from 1×10^{-3}
 415 to 5×10^{-4} mol/l, mainly due to the formation of C-S-H phases with different Ca:Si -ratios. Magnesium
 416 remained low ($< 10^{-5}$ mol/l) and was probably controlled by the presence and solubility of hydrotalcite and
 417 brucite at the studied times (Roosz et al. 2018, Bernard, 2017a, 2017b). Alkalis (Na and K) kept practically
 418 constant to concentrations of 4×10^{-3} and 1×10^{-4} , respectively. In turn, sulphate concentration remained below
 419 3×10^{-3} mol/l, controlled by ettringite solubility.

420 **Table 8.** pH evolution of studied concrete and micro-mortar (temperature = 20°C)

Age (days)	Concrete	Micro-mortar
	pH	
7	12.16	-
19	11.94	-
28	11.91	12.26
150	11.47	11.70
424	11.46	11.56
728	11.35	11.61

421

422 **Table 9.** Elemental composition of concrete pore solution after 150 and 450 days.

Water soluble ions [mg/l]	Concrete (150 d)	Concrete (450 d)
Al	0.70	0.01
Ca	50.87	20.82
Fe	0.14	0.00*
Mg	0.58	1.45
S	111.19	90.20
Si	50.53	40.75

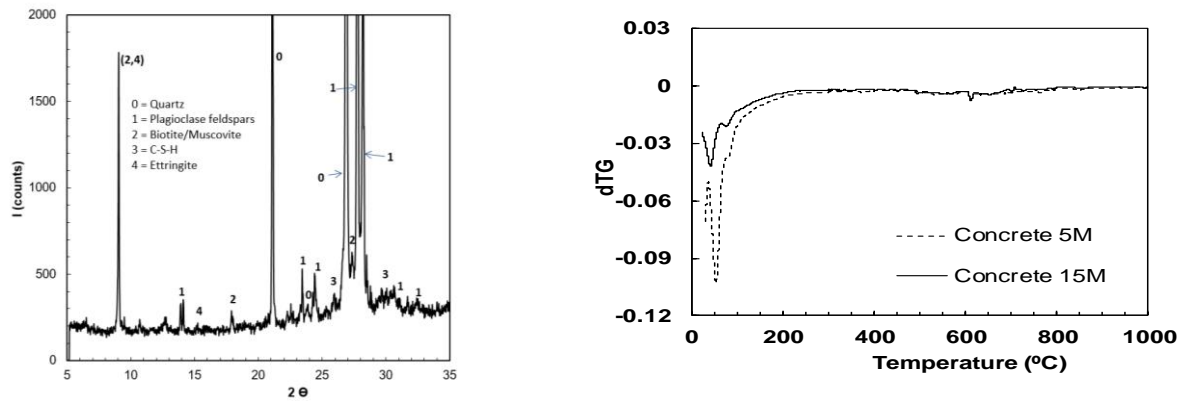
Na	101.17	115.25
K	52.01	39.93

423 *Under detection limit.

424 Full characterization of the micro-mortar was possible by using different complementary analytical
 425 techniques (XRD, TG-DSC, SEM-EDX, ²⁹Si and ²⁷Al MAS NMR, XAS), even identifying solid solutions like Cl- and
 426 Fe- bearing phases (which are normally present as minor phases in the hydrates). The same was true for the
 427 concrete, but in that case ²⁹Si and ²⁷Al MAS NMR were not applied. Specifically, the XAS studies were applied
 428 to identify in situ Fe- and Cl-containing phases present in these complex materials, which is novel for the
 429 studied compounds. Fe can substitute Al in various phases, thereby forming solid solutions which are difficult
 430 to be determined with other standard techniques. XAS has already been shown to be a good complementary
 431 technique providing molecular-level information for classical cements (Dilnesa et al., 2014, Vespa et al. 2015),
 432 but till the present moment, this technique has never been applied for the same purposes in low pH
 433 cementitious materials. Solid solutions properties differ significantly from the ones of pure components
 434 which could clearly influence the capability of retaining radionuclides by the low pH cementitious materials
 435 studied here (Bruno and Montoya, 2012; Dilnesa et al., 2014).

436 Identified assemblage phases for the concrete and the micro-mortar are summarized in Table 10. Quartz,
 437 feldspar, biotite and muscovite were identified by XRD as the main crystalline phase present as aggregates
 438 and quartz filler in the case of the concrete, as shown in Figure 3 left. C-S-H phases and other hydrates were
 439 more complicated to be identified with this technique due to their amorphous nature and the overlap of
 440 peaks, but C-S-H phases could be observed as broad bands. The XRD of the micro-mortar (no shown),
 441 presented very broad peaks, but calcite, quartz and unreacted alite and belite were able to be identified in
 442 agreement with the work of Vasconcelos et al. (2020). Calcium-silicate-hydrates (C-S-H) and calcium-
 443 aluminate-silicate-hydrates (C-A-S-H) were clearly identified with ²⁹Si and ²⁷Al MAS in the micro-mortar.
 444 Furthermore, ettringite was identified in both materials as a minor phase with the same techniques, although
 445 a slightly decomposition of ettringite could have happened due to sample preparation (see section 3.1). TG-
 446 DTA of both materials presented a mass loss around 100-300°C which was attributed to C-S-H phases and
 447 ettringite (Scrivener et al., 2018), as shown in Figure 3 for concrete after aging of 5 months and 15 months.
 448 However, in this temperature range the mass loss can also be attributed to water bound to mineral surfaces,
 449 making a quantification of the C-S-H phases difficult (Schöler et al., 2015). The water bound by the micro-
 450 mortar (11%) was calculated according to the method described in (Schöler et al. 2015). The weight loss at
 451 450 °C, indicative for portlandite was not observed, neither in micro-mortar nor in the concrete, in agreement
 452 with the measured pH (see Table 8). Additionally, the Ca/Si –ratio measured by SEM-EDX of the C-S-H phases
 453 were between 0.5-0.7 for both the concrete and the micro-mortar, with the Al/Si-ratio around 0.05. The ²⁹Si
 454 MAS NMR spectrum is depicted in Figure 4. A broad signal in the chemical shift range between -75 and -100
 455 ppm was the main signal of the spectrum and was assigned to the Si present in the C-(A)-S-H phases. The
 456 overlap of the signals did not allow unambiguous deconvolution but it is know that the spectra of C-S-H
 457 phases consists of at least three resonances called Q1, Q2(1Al) and Q2 (Lothenbach et al., 2012a; Richardson,
 458 1999, Vasconcelos et al. 2020). The main signal can also be overlapped with a minor signal of feldspar (-95 to
 459 -100 ppm). The signal at -69 ppm resulted from unreacted clinker (alite and belite). The broad feature at -110
 460 ppm is characteristic of unreacted silica fume and quartz filler.

461



462

463 **Figure 3:** X-ray diffractions (left) and differential thermogravimetric curves (right) for studied concrete

464

465

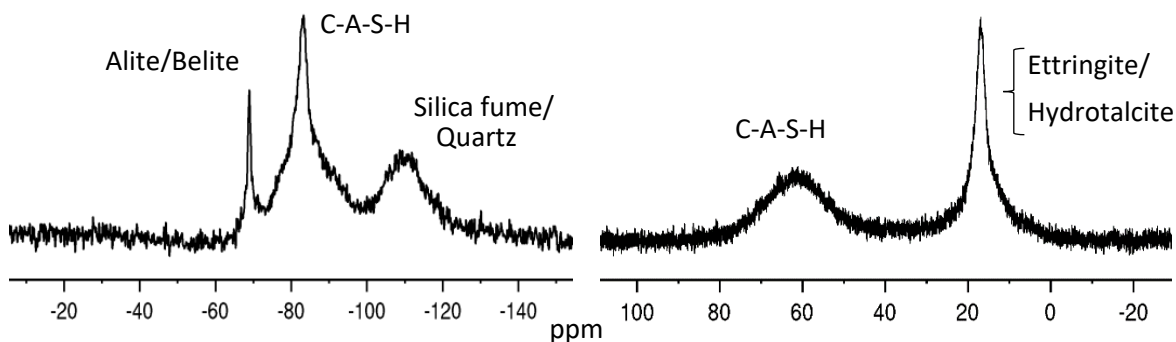
466

467

468

469

470

471 **Figure 4:** ^{29}Si MAS NMR spectra (left) and ^{27}Al MAS NMR spectra of the micro-mortar (right) in ppm.

472

473

474

475

476

The ^{27}Al -MAS-NMR spectrum (Figure 4) presented two different signals at 63.0 and 16.7 ppm, indicating that Al was in both octahedral and tetrahedral coordination (L'Hôpital et al., 2016). The observed tetrahedrally coordinated ^{27}Al resonances were associated with the aluminium in the bridging position of the C-S-H phases and feldspar, and the octahedral ^{27}Al with the presence of ettringite and probably hydroxalcite-like phases (Walkley and Provis, 2019).

477

478

479

480

481

482

483

484

485

486

487

488

489

Information on Fe speciation in both materials was studied by probing the Fe K-edge by XAS. The XANES is particularly sensitive to the type and number of neighbouring elements as well as bond distances and geometrical arrangement. For all samples and reference compounds, the XANES exhibited a feature at around 7114.5 eV (Figure 5) that derived predominantly from $1s \rightarrow 3d$ transitions. In O_h symmetry, this transition is forbidden, whereas in T_d symmetry the $1s(a_1) \rightarrow t_2$ transition is allowed (Westre et al., 1997). Thus, no pre-edge feature should be observed for octahedrally coordinated Fe. However, very weak features were still observed, and the intensity depended on the local symmetry and electronic properties of the cation. The intensity of the pre-edge was therefore low for common octahedral sites (e.g., hematite, goethite) and substantial for tetrahedral sites. The pre-edge of the micro-mortar and the concrete were located at a position similar to reference compounds, which contained only ferric iron. Therefore, the micro-mortar and the cement contain Fe(III). Furthermore, the intensity of the pre-edge of the micro-mortar seemed slightly larger as in the concrete, implying that the former contained substantial amounts of tetrahedral Fe^{3+} , but the latter only marginal amounts.

490

491

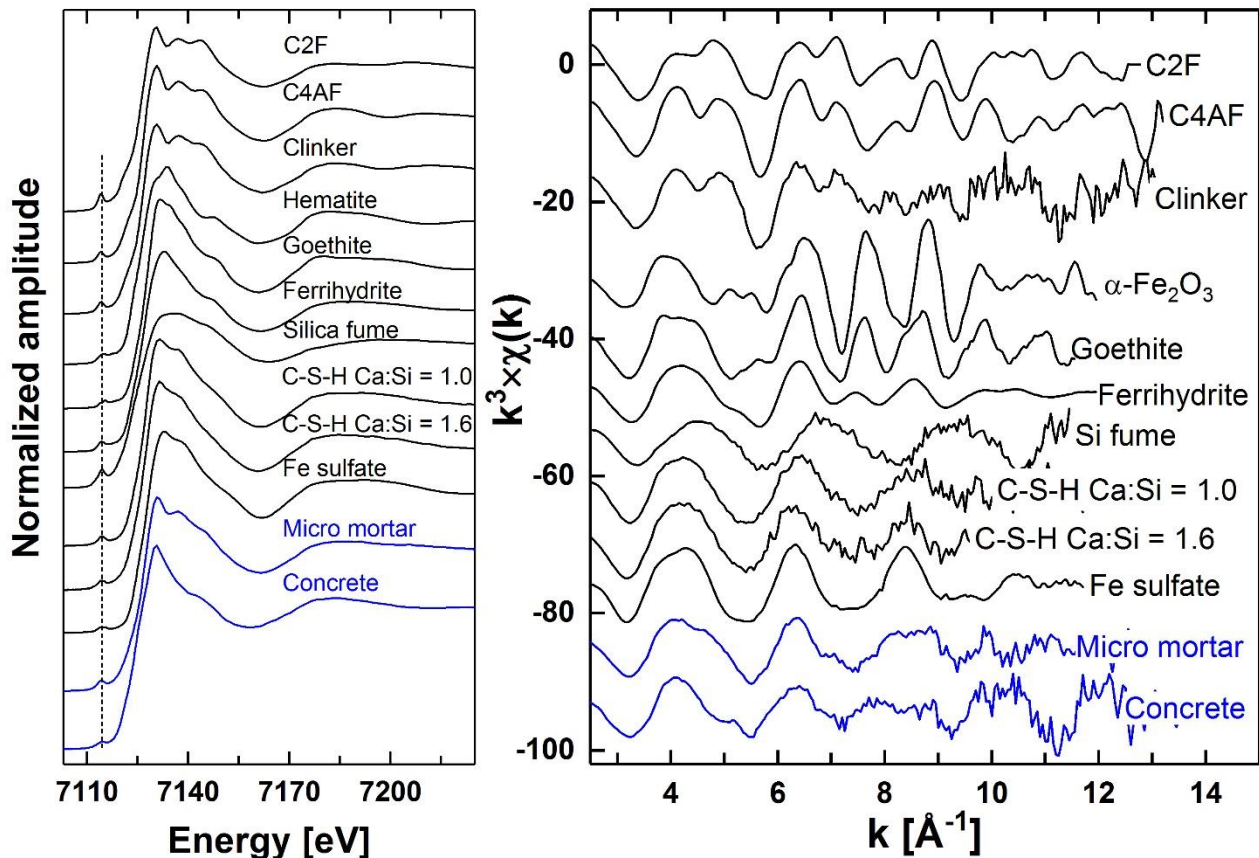
492

493

Further information was obtained from the analysis of the main absorption edge. The XANES of the reference compounds C2F and C4AF were very similar with the presence of two shoulders (~ 7137 and ~ 7145 eV) on the high-energy side of the main absorption edge. This finding can be explained by the crystallization of both compounds in the same crystal system (orthorhombic). The XANES of the clinker also bore similarities with

494 that of C2F and C4AF, pointing to the presence of these compounds or at least one of them in the clinker.
495 This finding compares well with reported data showing that the Fe-containing phases in the starting CEM I
496 clinker are C2F and C4AF. Similarly, the XANES of both C-S-H phases (doped with Fe(III)) bore similarities, only
497 the intensity of the shoulder after the main absorption edge slightly differed. The XANES of the micro-mortar
498 differed from the concrete, implying the location of Fe in different chemical environments. The XANES of the
499 former contained a shoulder, at ~ 7137 eV and weak feature at ~ 7145 eV, whereas the XANES of the second
500 is rather sharp and does not exhibit any significant feature. These findings may suggest the presence of ferrite
501 C2F and/or C4AF and possibly C-(F)-S-H phases in the micro-mortar, and the absence of these phases in the
502 concrete. Note that the XANES of C-(F)-S-H phases bear similarities with the reported XANES of siliceous
503 hydrogarnet (Dilnesa et al. 2014), suggesting that this phase may actually be present in the micro-mortar.
504 This finding would imply that the investigated micro-mortar and traditional ordinary Portland cement contain
505 the same thermodynamically stable Fe-containing phases. For the micro-mortar these results also agreed
506 with the observed intensity of the respective pre-edge features. The presence of minor amounts of other
507 compounds was impossible to exclude. The XANES of the concrete significantly differed from that of most
508 reference compounds. Though the XANES of ferrihydrite did not contain any shoulder, it differed from that
509 of the concrete, which did not exclude the presence of low amounts of this reference compound in the
510 sample.

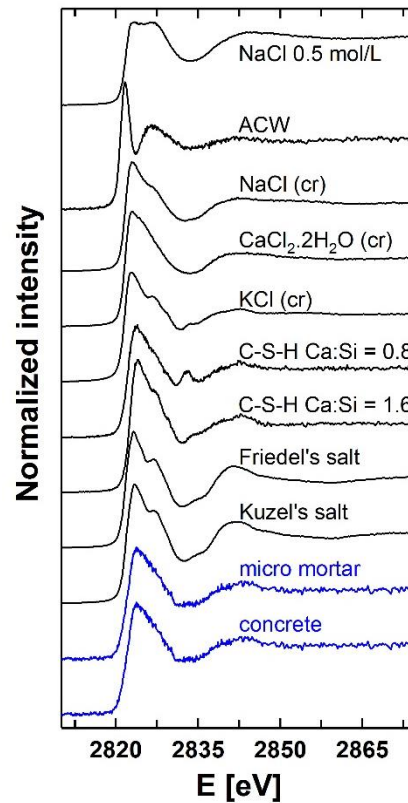
511 Extended X-ray absorption fine structure (EXAFS) spectra of C2F and C4AF were very similar and observed
512 differences in terms of oscillation amplitudes, was attributed to replacement of a fraction of Fe by Al within
513 the structure (Figure 5). Though noisier, the spectrum of the clinker also was similar to that of these reference
514 compounds. Likewise, the spectra of the C-(F)-S-H phases had similarities, suggesting closely related binding
515 environments. These findings agree with analysis of the XANES. Other important information was derived
516 from comparison of the spectra. The spectra of C2F, C4AF and the clinker had a first oscillation around 4.1 \AA^{-1} ,
517 like most reference compounds, and a second oscillation or shoulder at $\sim 4.8 \text{ \AA}^{-1}$ (Colville and Geller, 1971).
518 Recently reported EXAFS spectra for ferric saponite, a smectite containing Fe^{3+} at tetrahedral position, exhibit
519 oscillat (Finck et al., 2019), thus strengthening the attribution of this spectral feature to tetrahedral ferric
520 iron. The EXAFS spectrum of the micro-mortar mainly differed from that of the concrete in the spectral
521 features in the $4 - 6 \text{ \AA}^{-1}$ range. Still, both had an oscillation amplitude maximum at $\sim 4.1 \text{ \AA}^{-1}$, implying the
522 presence of octahedral Fe^{3+} . The spectrum of the micro-mortar had a shoulder at $\sim 4.7 \text{ \AA}^{-1}$ which was absent
523 in the spectrum of the cement, whereas the spectrum of the cement had a feature at $\sim 5.2 \text{ \AA}^{-1}$ which was
524 absent in the spectrum of the micro-mortar. By comparison with reference compounds, only spectra of C2F,
525 C4AF and the clinker had a shoulder at $k \sim 4.8 \text{ \AA}^{-1}$, signifying that at least a fraction of Fe in the micro-mortar
526 was located in an environment similar to that of these reference compounds. Interestingly, this result also
527 agreed with the shoulder at $k \sim 7 \text{ \AA}^{-1}$ in the spectrum of the micro-mortar, because all other reference
528 compounds had an oscillation amplitude minimum at this k value. Other possible Fe-bearing phases present
529 in the micro-mortar may be C-(F)-S-H phases (Mancini et al. 2020), whereas hematite and goethite are clearly
530 excluded. Results thus pointed to the presence of Fe in various environments in the sample, corroborating
531 conclusions obtained by analysis of the XANES. Note that XANES and EXAFS spectroscopy both exclude the
532 presence of detectable amounts of ferrous (Fe(II)) or elemental iron. Observed differences in Fe speciation
533 between both compounds can only be attributed to the presence of low amounts of Fe in the aggregates.
534 Furthermore, only octahedral ferric iron Fe(III) was detected in the concrete although in this case no clear
535 phases could be identified.



536

537 **Figure 5:** Fe K-edge XANES (left) and EXAFS spectra (right) of the micro-mortar, the concrete and the
 538 reference compounds. The vertical dashed line in the XANES indicates the position of the pre-edge features.

539 For chlorine, only Cl K-edge XANES were recorded for the micro-mortar, the concrete and reference
 540 compounds (Figure 6). The XANES of the liquid reference compounds differed significantly from that of all
 541 solid compounds. For the solid compounds, the maximum of the main absorption edge was located at similar
 542 energy position, implying that all compounds contained chloride ions. Friedel's and Kuzel's salt have very
 543 similar XANES with a shoulder at ~ 2827 eV, hinting at comparable environments. The XANES of both C-S-H
 544 phases differed: the XANES of the phase with higher Ca content had a weak shoulder at ~ 2827 eV, whereas
 545 the XANES of the phase with higher Si content exhibited a distinctive feature at ~ 2833 eV. The XANES of the
 546 sodium, calcium and potassium chloride differed from each other, in agreement with differences in their
 547 crystal structures. XANES of the micro-mortar and the concrete were very similar. This result hinted at
 548 comparable Cl environments in the samples, and excluded the presence of significant amounts of reference
 549 compounds such as C-S-H phases, Kuzel's and Friedel's salts, NaCl and KCl. The XANES of $\text{CaCl}_2 \cdot 2\text{H}_2\text{O}$ bore
 550 similarities with the samples, however the absorption edge was wider and higher in amplitude. Consequently,
 551 Cl can only be bound, physically or chemically, to another mineral phase present in the samples. Additional
 552 reference compounds would be needed to identify the Cl binding environment in the micro-mortar and in
 553 the cement.



554

555 **Figure 6:** Cl K-edge XANES of the micro-mortar, the cement and reference compounds.556 **Table 10.** Hydrates and raw materials identified (Id.) / quantified in the concrete and the micro-mortar

	Concrete	Micro-mortar
<i>Hydration phases</i>		
C-(A)-S-H	Id.*	Id.*
C-(F)-S-H	Not observed	Id.
Ettringite	Id. (minor)	Id. (minor)
Hydrotoalcite	Not observed	Id.
Friedel's salt	Not present	Not present
Kuzel's salt	Not present	Not present
Bound water	Not determined	11%
<i>Raw materials</i>		
Alite/Belite	Not observed	Id.
Ferrites	Not observed	C2F ^a /C4AF ^b
Blast furnace slag	Id.	Id.
Quartz filler	Id.	Id.
Calcite	Not observed	< 2.0 wt. %
Silica Fume	Id.	Id.

557

*Ca/Si ratio =0.5-0.7 and Al/Si-ratio = 0.05

558

^a Dicalcium ferrite [Ca₂Fe₂O₅]

559

^b Tetracalcium aluminoferrite [Ca₂FeAlO₅]

560

561 **4.5 Percolation experiments with concrete**562 Percolation experiments were performed with the concrete and using two different water compositions,
563 Granitic II and Clay II, representing the dilute Grimsel groundwater (pH = 9.7) and the FEBEX bentonite

564 porewater (pH = 8.0), respectively. Table 11 shows that the evolution of the pH (within 1 cm depth) as a
 565 function of time is kept approximately constant during 660 days and with values similar to the pH of the
 566 water injected. This observation indicates that at the high pressure of the injected water, chemical
 567 equilibrium with the cement hydrates has not been produced. Very low hydraulic conductivities of 1×10^{-13}
 568 m/s were also obtained with the same percolation experiments as a function of time and independently of
 569 the water used. This low value is in agreement with the low porosity measured for this material (see Table
 570 7). It was also observed that only at exposure times > 600 days the hydraulic conductivity diminishes to 1×10^{-14}
 571 m/s probably indicating decreasing of porosity due to precipitation reactions.

572 Regarding the chemical composition of the cement paste of the concrete after > 600 days of exposure to
 573 both waters indicates a clear change in the CaO/SiO₂-ratio that occurs similarly with both waters. In addition
 574 a clear increase in Mg was observed in the sample exposed to the Clay II water. The formation of a calcite
 575 layer (<10µm) on the surface in contact with the water is also detected in all cases, although a less
 576 homogenous distribution was observed when using the clay water, similarly as observed by Garcia-Calvo et
 577 al. (2010) .

578

579 **Table 11.** pH development of studied concrete and the micro-mortar in various temperatures, groundwater
 580 exposures and measurement set-ups. Values in brackets indicate the volume of percolated water.

Temp.	20°C	20°C	20°C	20°C	20°C	20°C	10°C	95°C	95°C
Solution	Granitic I	Granitic II	Clay I	Clay II	Saline	Bentonite	Granitic III	Granitic III	B75
Method	Leaching	Percolation	Leaching	Percolation	Leaching	Leaching	Leaching	Leaching	Leaching
Sample	Micro-mortar	Concrete	Micro-mortar	Concrete	Micro-mortar	Micro-mortar	Micro-mortar	Micro-mortar	Micro-mortar
Time (days)	pH								
29	11.33		10.67		11.02				
30	11.42		10.89		11.15				
31	11.47		11.11		11.24				
32	11.35		11.05		11.14				
33	11.44		11.13		11.2				
37	11.37		11.21		11.29				
45							12.31		
58	11.13		10.93		10.87				
88	10.81		10.54		10.66				
120	10.64		10.48		10.74				
155	10.46		10.23		10.56				
175							11.96	11.02	
180	10.39		10.21		10.51	10.07**			
210									
211	10.38		10.24		10.39				
265	10.52		10.17		10.55				
322							11.87	10.8	10.85
329	10.68		10.14		10.64				
330									
394	10.73	9.3* (17 ml)	10.25	8.2* (51 ml)	10.47				
450									
455							11.75	11.57	

480		9.2* (8 ml)		8.2* (56 ml)					
540									
567							11.48	10.8	10.67
660		8.9* (7 ml)		8.2* (25 ml)					

581 *Within 1cm depth. **water composition (mg/L): Si (12.2), Mg (1.4), Na (3832), K (167), Ca (412), Cl (627),
582 SO₄ (8783), Al (1.46)

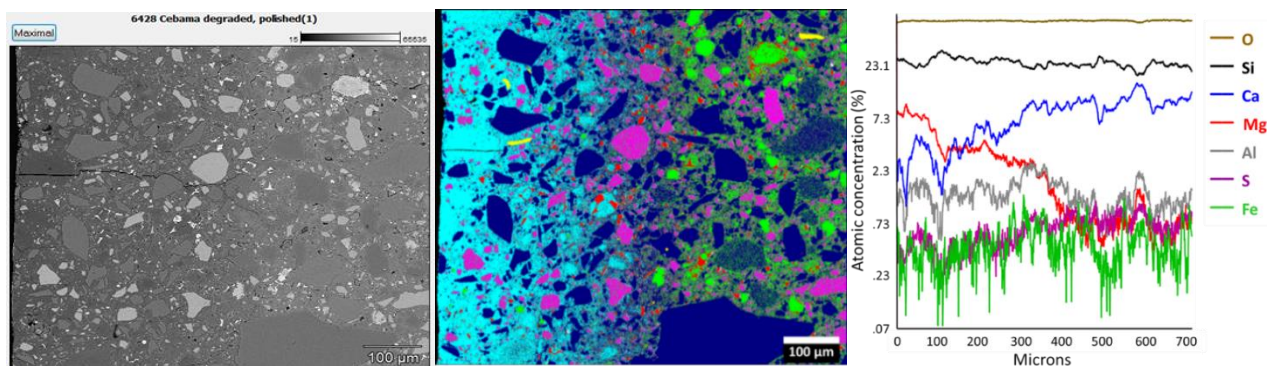
583

584 4.6 Leaching experiments with the micro-mortar

585 Leaching experiments at ambient temperature (20°C) were performed with the micro-mortar and using four
586 different water compositions given in Table 3 (Granitic I, Clay I (Callovo-Oxfordian), Saline (granitic) and
587 Bentonite (MX-80)). Although the experimental setup used with the bentonite was slightly different, similar
588 evolution of water pH as a function of time was observed (Table 11). The pH of all the waters increased to
589 pH ~ 10.1 - 10.5 after 180 days of reaction due to the leaching and dissolution of the micro-mortar in the
590 aqueous solution. No apparent changes of pH were observed at longer times of interaction. In the case of
591 the experiments performed with bentonite the chemical composition of the bentonite solution after 6
592 months of exposure was also measured (see Table 11). These results clearly show notable changes of cation
593 concentration in the aqueous solution, especially for Mg and Al. Specifically, Mg concentration decreased
594 and Al, although present in very low concentrations, increased two orders of magnitude. Other significant
595 changes were related to the increase and decrease of one order of magnitude of the sulphate and chloride
596 concentration, respectively. In minor degree, silicon concentration increased possible indicating dissolution
597 of C-(A)-S-H phases.

598 In order to have a deeper understanding of the processes happening, post-mortem analysis by SEM-EDX of
599 the micro-mortar in contact with the different waters was also done. In addition, in order to help to identify
600 the chemical processes occurring in that area, the cross section of the sample used with bentonite was
601 analysed (homogenised 700 µm) giving the elemental depth profile depicted in Figure 7 (right). Hollow shell
602 pores having sizes in the range of about 1-15 µm were identified. These pores were embedded in cement gel
603 and appeared to be connected to the continuous capillary pore system by much smaller gel pores. From the
604 images it can be clearly seen that the sample had an initial heterogeneous mineralogical composition. (in the
605 studied spatial scale), identifying calcium-(aluminato)-silicate-hydrate phases, blast furnace slag, quartz filler
606 and initial clinker (belite, ferrite) by using the false colour technique..

607



608 **Figure 7:** Cross-section of micro-mortar after contact with bentonite pore water by SEM-EDX. Phase
609 distributions in false colours (centre) overlaying the backscattered electron image presenting a material
610 contrast of micro-mortar (left). Left side at images: surface of cement. Mg-exchanged C-S-H (cyan,
611 C/S=0.17), quartz filler (blue), MgAlCa₄Si₃O_xH_y (pink), belite (green), tetracalcium aluminoferrite (red),

612 *muscovite (yellow). Note that the crack observed in the figure was produced during the cutting of the*
613 *sample after the degradation experiments. Elemental depth profile extracted from SEM-EDX map data*
614 *(right).*

615

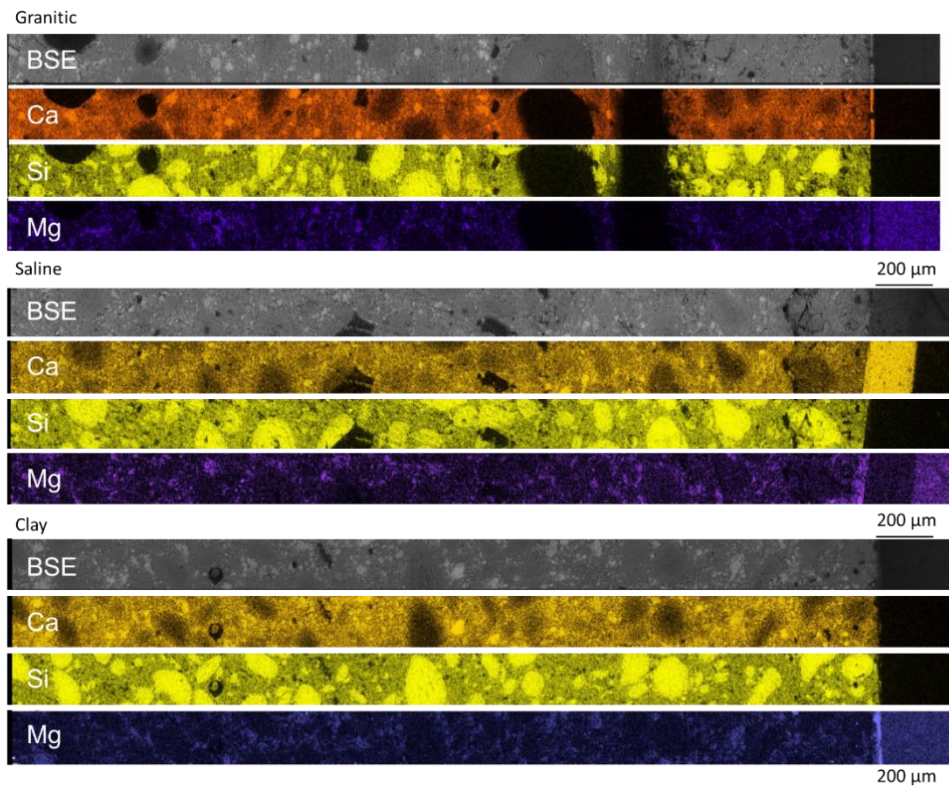
616 Although, contact time with the four waters was different, similar processes were identified in all cases and
617 explained in the following. A clear reaction front was observed in the micro-mortar in contact with the four
618 waters (Figures 7 and 8). In the case of the experiment performed with bentonite (180 contact days), the
619 reacting front was 400 μm from the surface. In all the cases, calcium content was depleted in this area
620 compared to non-affected internal parts of the samples. In groundwater compositions containing substantial
621 magnesium concentrations (Clay I and Bentonite), a magnesium enrichment was observed in the reaction
622 front (Figure 7 and Figure 8). This process is mainly occurring due to the high gradient in Mg concentration
623 between (the bentonite and Clay I) waters and the cement solid. Magnesium diffused into the solid sample
624 and accumulated at the interface, probably sorbing on silicate structures or precipitating as new Mg
625 structures (Bernhard et al. 2018b). As recently described in the literature (Dauzeres et al. 2016, Bernard et
626 al. 2018a, 2020a, González-Santamaria et al. 2020), this magnesium enrichment starts with the pH decrease
627 and chemical destabilization of the C-S-H phases and their partial decalcification and release of calcium. Due
628 to the Ca:Si decrease, more amorphous silica structure are present which possibly favours the formation of
629 M-S-H phases (Bernard et al. 2017) which clearly have different chemical structure than C-S-H phases (Roosz
630 et al. 2015, 2016, Bernhard et al., 2019a, 2019b, 2020b). However, the nature and the structure of the
631 magnesium bearing phases in the enriched zone could not be elucidated by the experimental techniques
632 used in this work. In the case of the bentonite experiment, magnesium concentration close to the surface
633 was three times higher than calcium suggesting the formation of magnesium-silicate-hydrate phases by
634 decalcification of the C-S-H phases. This would agree with the observed decreasing atomic ratio with the
635 distance. At 140 μm the Mg/Ca -ratios were equal and at 400 μm the Ca/Mg-ratio kept constant and equal
636 to the initial ratio, suggesting that the reactive front during 6 months was 400 μm . This observed processes
637 were similar to the ones described in Mäder et al. (2017) when describing the interface between a low-pH
638 concrete and Opalinus clay in an in-situ experiment.

639 Other cation exchange with calcium, observed when using Bentonite water, was Na, which was present
640 initially in high concentration in the water ($\sim 0.25\text{M}$) and decreased after 6 month interaction. In addition,
641 the elemental depth profile showed a decrease of sulphate in the altered zone in agreement with the increase
642 of sulphate in the bentonite water. Apart from these main processes, it seems also obvious that the clinker
643 (belite and ferrite) was hydrating/reacting in the magnesium exchanged zone with the aqueous solution to
644 form magnesium containing phases (i.e. M-S-H phases). It can be seen that the blast furnace slag and the
645 quartz filler remained in the samples as non-reactive solids or presenting a slow kinetic dissolution.

646 Precipitation of calcite and gypsum had only been observed on the holes present in the surface in contact
647 with the bentonite water and not in the pore structure. The formation of a solid containing calcium was also
648 observed at the surface of the solid sample, when the saline groundwater was used. It is likely that the
649 formation of these solid in the surface decreased the rate of magnesium penetration into the micro-mortar,
650 as a difference between clay- and saline groundwater was observed.

651 Finally leaching experiments at different temperatures (10°C and 95°C) with the Granitic III and bentonite
652 B75 water were performed. Differences on the measured pH at different temperatures, but using the same
653 Granitic III water, was observed, most probably due to the influence of temperature on the pH values. On
654 the other hand pH values obtained at 95°C with both, granitic and B75 waters gave very similar values,
655 indicating that similar reactions are occurring with both waters at this temperature. For micro-mortar
656 samples in direct contact with bentonite slurry (B75) at both temperatures, a calcium enrichment

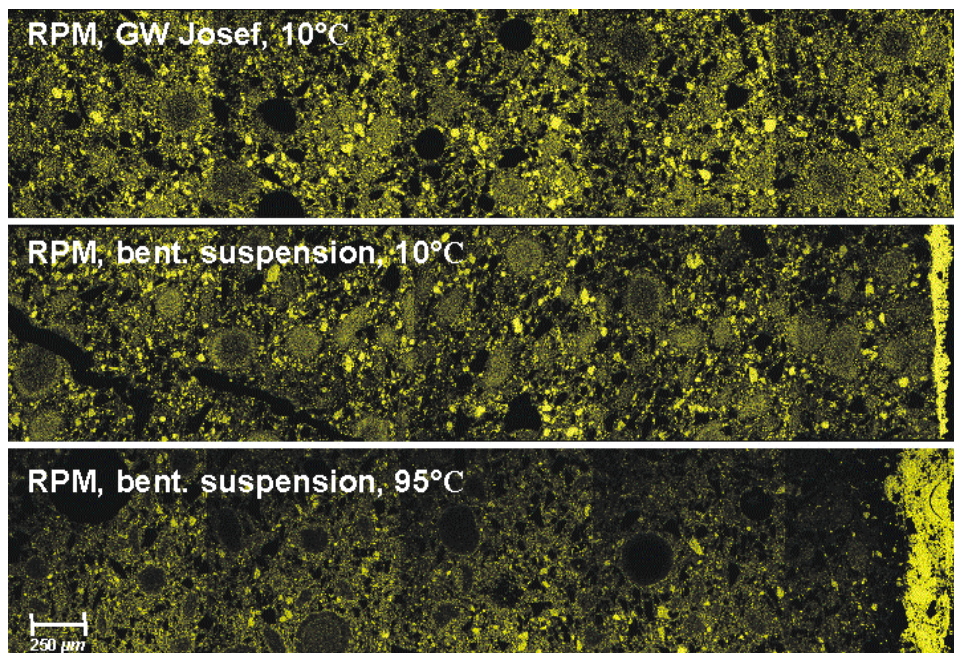
657 (precipitation) was observed in the surface (Figure 9) being more pronounced at 95°C within the studied
 658 timescales (567 days). Other major changes were not identified when using the Granitic III water at 10°C.



659

660 **Figure 8:** Scanning elemental maps of Ca, Si and Mg in micro-mortars exposed to Granitic I, Saline and Clay I
 661 -groundwater.

662



663

664 **Figure 9:** Scanning electron images with Ca elemental map (yellow) showing the calcium enrichment at the
 665 interaction boundary with Granitic III (top), bentonite suspension (water B75) at 10 (middle) and 95°C
 666 (bottom).

667

668 **5. CONCLUSIONS**

669 A new designed slag-based "low-pH" concrete and micro-mortar have been manufactured and characterized
670 within the Cebama project in order to be used as a reference material in different experiments and modelling
671 work. Several experimental techniques available in different laboratories around Europe have provided
672 mechanical, hydraulic and geochemical properties of these new materials as a function of time. Compressive
673 strengths, pore solution pH and pH development were comparable to fly ash and silica fume based "low-pH"
674 mix designs on the basis of literature.

675 The compressive strengths of the concrete and micro-mortar were very high and comparable to high
676 performance concretes. Microstructural analyses showed dense and homogeneous microstructures with low
677 porosity mainly in the nanoscale range providing very low hydraulic conductivities. Chemical characterisation
678 of the micro-mortar identified C-S-H and C-(A)-S-H phases as the main hydrates. Ca/Si ratio were between
679 0.5-0.7 and Al/Si-ratio around 0.05 for these solid phases. Minor phases were ettringite and hydrotalcite and
680 the pore solution pH was below the saturation pH of portlandite, in agreement with the solid characterization
681 and other "low-pH" formulations described in the literature. XAS analysis provided information on Fe and Cl
682 speciation for the first time in this kind of low-pH cementitious materials. The data suggest that the Fe
683 environment in the micro-mortar differed from that in the concrete, and that Fe was present only as ferric
684 iron in both materials. In the micro-mortar, Fe was present at both tetrahedral and octahedral sites. Binding
685 environments may be similar to that in C2F or C4AF, and possibly C-(F)-S-H phases. In the concrete, data
686 suggest that Fe predominated at octahedral sites. Upcoming modelling of EXAFS data will provide additional
687 information in terms of the nature and numbers of neighbouring atoms and bond distances. On the other
688 hand, XAS pointed to a similar binding environment for Cl in the micro-mortar and cement, and ruled out the
689 presence of Cl in an environment comparable to that in the liquid phase. Data also excluded the presence of
690 Cl in an environment comparable to that in Kuzel's or Friedel's Salt and Cl incorporated in C-S-H phases. The
691 use of additional reference compounds would be needed to obtain information on Cl speciation.

692 Alteration of the micro-mortar in contact with different representative pore- and groundwaters in nuclear
693 waste disposal, was observed within relatively short exposure times compared to the lifetime of a repository.
694 However, should be kept in mind that high solid/liquid ratios were used to accelerate the laboratory leaching
695 experiments that are not representative of real repository scenarios. In all the cases, calcium content was
696 depleted in the alteration zone of the solid compared to non-affected internal parts of the samples. Micro-
697 mortar in contact with magnesium containing porewaters, specifically with clay and bentonite waters, at
698 20°C, shows a Mg enrichment through the solid, due to a significant chemical gradient between both
699 materials. Possible precipitation of Mg phases, such M-S-H phases with complex chemical structures or
700 brucite occurred in this zone. This was not observed when granitic waters was used. Calcium depletion and
701 magnesium enrichment at the reaction front is not a unique quality of slag-based "low-pH" mix designs.
702 Similar reaction front has been observed also in fly ash and silica fume based "low-pH" mix designs in contact
703 with clays in field and laboratory experiments.

704 All these results clearly show that the performance of "low-pH" mix designs of this work exceeds the
705 performance of traditional Portland cement concretes and are comparable to high performance concretes.
706 "Low-pH" mix designs are thus very suitable construction materials, if the mix design is performed
707 accordingly and the mixing methodology and emplacement method results in a homogeneous mix. In
708 addition, it can be deduced that slag is able to replace fly ash when producing ternary "low-pH" mixtures in
709 the future, if needed due to material supply or quality problems. Other interesting results are related to the
710 use of XAS techniques to identify minor phases in cementitious systems.

711

712 **ACKNOWLEDGEMENTS**

713 The research leading to these results has received funding from the European Union's European Atomic
 714 Energy Community's (Euratom) Horizon 2020 Programme (NFRP-2014/2015) under grant agreement, 662147
 715 - "Cebama". V. Montoya acknowledge the German Federal Ministry of Education and Research (Grant
 716 02NUK053A) and the Initiative and Networking Fund of the Helmholtz Association (Grant SO-093) within the
 717 iCross project for partial funding. Additionally, KIT-INE acknowledges the ESRF and the KIT Synchrotron Light
 718 Source for provision of synchrotron radiation beam time and D. Banerjee for assistance during measurements
 719 at the BM26A beamline. We thank B. Lothenbach (EMPA, Switzerland) and S. Grangeon (BRGM, France) for
 720 providing reference compounds for the XAS study. The authors also acknowledge the support provided by
 721 many supervisors and technical experts during the course of this work: Dieter Schild, Thorsten Schäfer,
 722 Christian Adam, Kathy Dardenne and Jörg Rothe from KIT; A. Fernandez and J.L. Garcia-Calvo from CSIC; M.
 723 Felipe-Sotelo and M. Isaacs from University of Surrey; Tomáš Rosendorf from ÚJV Řež, a. s.; John Provis and
 724 Neil Hyatt from University of Sheffield; Mia Löija and Hanna Litti from VTT and four anonymous reviewers for
 725 their careful reading of the paper and their many insightful comments and suggestions.

726 **REFERENCES**

- 727 Alonso, M.C., Garcia Calvo, J.L., Walker, C., 2012. Development of an accurate pH measurement
 728 methodology for the pore fluids of low pH cementitious materials. SKB report R-12-02, Sweden.
- 729 ANDRA (2005) Argile, synthesis evaluation of the feasibility of a geological disposal in an argillaceous
 730 formation (2005) <https://international.andra.fr/> (accessed 17.07.20)
- 731 Bach, T.T.H., 2010. Physico-chemical evolution of low-pH cements : influence of the temperature and the
 732 retention mechanism of alkalins. Thesis, Université de Bourgogne.
- 733 Bernard, E. 2017a. Magnesium silicate hydrate (M-S-H) characterization: temperature, calcium, aluminum
 734 and alkali. Thesis. Université Bourgogne Franche-Comté. France
- 735 Bernard, E., Dauzères A., Lothenbach, B., 2018b. Magnesium and calcium silicate hydrates, Part II: Mg-
 736 exchange at the interface "low-pH" cement and magnesium environment studied in a C-S-H and M-S-
 737 H model system, Applied Geochemistry, 89, 210-218
- 738 Bernard, E., Jenni, A., Fisch, M., Grolimund, D., Mäder U. 2020a. Micro-X-ray diffraction and chemical
 739 mapping of aged interfaces between cement pastes and Opalinus Clay. Applied geochemistry, 104538
- 740 Bernard, E, Lothenbach, B., Cau-Dit-Coumes, C., Chlique, C., Dauzères, A., Pochard, I. 2018a. Magnesium and
 741 calcium silicate hydrates, Part I: Investigation of the possible magnesium incorporation in calcium
 742 silicate hydrate (CSH) and of the calcium in magnesium. Applied Geochemistry 89, 229-242
- 743 Bernard, E., Lothenbach, B., Chlique, C., Wyrzykowski, M., Dauzères, A., Pochard, I., Cau Dit-Coumes. 2019b.
 744 Characterization of magnesium silicate hydrate (MSH). Cement and concrete research 116, 309-330
- 745 Bernard, E., Lothenbach, B., Le Goff, F. Pochard, I., Dauzères A. 2017c. Effect of magnesium on calcium
 746 silicate hydrate (CSH) Cement and Concrete Research 97, 61-72
- 747 Bernard, E. Lothenbach, B., Rentsch, D., Pochard, I., Dauzères A., 2017b Formation of magnesium silicate
 748 hydrates (MSH) Physics and Chemistry of the Earth, Parts A/B/C 99, 142-157
- 749 Bernard, E., Lothenbach, B., Cau-Dit-Coumes, C., Pochard, I., Rentsch D. 2020b. Aluminum incorporation
 750 into magnesium silicate hydrate (MSH) Cement and concrete research 128, 105931
- 751 Bernard, E., Lothenbach, B., Pochard, I., Cau-Dit-Coumes C. 2019a. Alkali binding by magnesium silicate
 752 hydrates Journal of the American Ceramic Society 102 (10), 6322-6336
- 753 Borghel-Bouny, V., Andrade, C., Torrent, R., Scrivener, K., 2007. Durability indicators: relevant tools for

- 754 performance-based evaluation and multi-level prediction of RC durability, in Baroghel et al.
755 Proceedings : International RILEM Workshop on Performance Based Evaluation and Indicators for
756 Concrete Durability , pro047
- 757 Bradbury, M.H., Baeyens, B., 2011. Physico-chemical characterisation data and sorption measurements of
758 Cs, Ni, Eu, Th, U, Cl, I and Se on MX-80 bentonite. PSI report 11-05, Switzerland.
- 759 Bruno, J., Montoya, V., 2012. From aqueous solution to solid solutions: A process oriented review of the
760 work performed within the FUNMIG project. *Appl. Geochemistry* 27, 444–452.
761 <https://doi.org/10.1016/J.APGEOCHEM.2011.09.013>
- 762 Cau Dit Coumes, C., Courtois, S., Nectoux, D., Leclercq, S., Bourbon, X., 2006. Formulating a low-alkalinity,
763 high-resistance and low-heat concrete for radioactive waste repositories. *Cem. Concr. Res.* 36, 2152–
764 2163. <https://doi.org/10.1016/j.cemconres.2006.10.005>
- 765 Codina, M., Cau-dit-Coumes, C., Le Bescop, P., Verdier, J., Ollivier, J.P., 2008. Design and characterization of
766 low-heat and low-alkalinity cements. *Cem. Concr. Res.* 38, 437–448.
767 <https://doi.org/10.1016/J.CEMCONRES.2007.12.002>
- 768 Colville, A.A., Geller, S., 1971. The crystal structure of brownmillerite, $\text{Ca}_2\text{FeAlO}_5$. *Acta*
769 *Crystallogr. Sect. B* 27, 2311–2315. <https://doi.org/10.1107/S056774087100579X>
- 770 Czech Geological Institute, 1987. *Metodiky laboratorních zkoušek v mechanice zemin a hornin (Methods of*
771 *laboratory testing in soil and rock mechanics)*. Prague.
- 772 Dauzères, A., Achiedo, G., Nied, D., Bernard, E., Alahrache, A., Lothenbach B. 2016. Magnesium
773 perturbation in low-pH concretes placed in clayey environment—solid characterizations and modeling
774 *Cement and Concrete Research* 79, 137-150
- 775 Dauzères, A., Le Bescop, P., Cau-Dit-Coumes, C., Brunet, F., Bourbon, X., Timonen, J., Voutilainen, M.,
776 Chomat, L., Sardini, P., 2014. On the physico-chemical evolution of low-pH and CEM I cement pastes
777 interacting with Callovo-Oxfordian pore water under its in situ CO₂ partial pressure. *Cem. Concr. Res.*
778 58, 76–88. <https://doi.org/10.1016/J.CEMCONRES.2014.01.010>
- 779 Dilnesa, B.Z., Wieland, E., Lothenbach, B., Dähn, R., Scrivener, K.L., 2014. Fe-containing phases in hydrated
780 cements. *Cem. Concr. Res.* 58, 45–55. <https://doi.org/10.1016/J.CEMCONRES.2013.12.012>
- 781 Dole, L.R., Mattus, C.H., 2007. Low pH concrete for use in the US high-level waste repository: Part I
782 overview, in: *Proceeding 2nd Workshop R&D on Low PH Cement for a Geological Repository*, Madrid,
783 Spain, June. pp. 15–16.
- 784 Engelhardt, G., Michel, D., 1987. *High-resolution solid-state NMR of silicates and zeolites*. John Wiley and
785 Sons, New York, NY, United States.
- 786 Finck, N., Schlegel, M.L., Dardenne, K., Adam, C., Kraft, S., Bauer, A., Robert, J.-L., 2019. Structural iron in
787 smectites with different charge locations. *Phys. Chem. Miner.* 46, 639–661.
788 <https://doi.org/10.1007/s00269-019-01028-y>
- 789 Gaboreau, S., Prêt, D., Tinseau, E., Claret, F., Pellegrini, D., Stammose, D., 2011. 15 years of in situ cement–
790 argillite interaction from Tournemire URL: Characterisation of the multi-scale spatial heterogeneities
791 of pore space evolution. *Appl. Geochemistry* 26, 2159–2171.
792 <https://doi.org/https://doi.org/10.1016/j.apgeochem.2011.07.013>
- 793 Gallé, C., 2001. Effect of drying on cement-based materials pore structure as identified by mercury
794 intrusion porosimetry: A comparative study between oven-, vacuum-, and freeze-drying. *Cem. Concr.*
795 *Res.* 31, 1467–1477. [https://doi.org/10.1016/S0008-8846\(01\)00594-4](https://doi.org/10.1016/S0008-8846(01)00594-4)
- 796 Garcia-Calvo, J.L., Hidalgo, A., Alonso, C., Fernandez Luco, L., 2010. Development of low-pH cementitious

- 797 materials for HLRW repositories. Resistance against ground waters aggression. *Cem. Concr. Res.* 40,
798 1290–1297. <https://doi.org/10.1016/j.cemconres.2009.11.008>
- 799 Garcia, J.L., Alonso, M.C., Hidalgo, A., Luco, L., Fernández, 2007. Design of low-pH cementitious materials
800 based on functional requirements, in: *Proceedings R&D on Low-PH Cement for a Geological*
801 *Repository, 3rd Workshop, June.* pp. 13–14.
- 802 Gascoyne, M., 2002. Influence of grout and cement on groundwater composition. Working Report 2002-07,
803 POSIVA, Finland
- 804 González-Santamaría D.E., Fernández R., Ruiz A.I., Ortega A., Cuevas J 2020 . High-pH/low pH ordinary
805 Portland cement mortars impacts on compacted bentonite surfaces: Application to clay barriers
806 performance. *Applied Clay Science*, 193, 105672
- 807 Holt, E., Claret, F., Mäder, U., 2016. Report on WP1 selected experimental materials to be used, including
808 both new laboratory and aged in-situ samples. CEBAMA Deliverable D1.05.
- 809 Holt, E., Koho, P., 2016. POPLU Experimental summary report. DOPAS project, Deliverable D4.5.
- 810 Holt, E., Leivo, M., Vehmas, T., 2014. Low-pH concrete developed for tunnel end plugs used in nuclear
811 waste containment, in: *Concrete Innovation Conference (CIC2014).* 11 - 13 June 2014, Oslo.
- 812 Idiart, A., Lavina, M., Kosakowski, G., Cochepein, B., Meeussen, J., Samper, J., Mon, A., Montoya, V., Munier,
813 J., Poonoosami, J., Montenegro, L., Deissman, G., Rohmen, S., Hax Damiani, L., Coene, E., Nieves, A.,
814 2020. Reactive transport modelling of a low-pH concrete / clay interface. *Appl. Geochemistry*, 115,
815 104562
- 816 Koskinen, K., 2014. Effects of Cementitious Leachates on the EBS. Posiva Oy 31.
- 817 L'Hôpital, E., Lothenbach, B., Kulik, D.A., Scrivener, K., 2016. Influence of calcium to silica ratio on
818 aluminium uptake in calcium silicate hydrate. *Cem. Concr. Res.* 85, 111–121.
819 <https://doi.org/10.1016/J.CEMCONRES.2016.01.014>
- 820 Lagerblad, B., Trägårdh, J., 1994. Conceptual model for concrete long time gradation in a deep nuclear
821 waste repository. SKB Technical report, 95-21, Sweden
- 822 Leivo, M., Vehmas, T., Holt, E., 2014. Developing Low pH concrete for tunnel plugging structures in nuclear
823 waste containment, in: *XIII Nordic Concrete Research Symposium - Reykjavik, Iceland Duration: 13*
824 *Aug 2014 → 15 Aug 2014.* pp. 491–494.
- 825 Leroy, P., Hördt, A., Gaboreau, S., Zimmermann, E., Claret, F., Bücken, M., Stebner, H., Huisman, J.A., 2019.
826 Spectral induced polarization of low-pH cement and concrete. *Cem. Concr. Compos.* 104, 103397.
827 <https://doi.org/10.1016/J.CEMCONCOMP.2019.103397>
- 828 Lothenbach, B., Le Saout, G., Ben Haha, M., Figi, R., Wieland, E., 2012a. Hydration of a low-alkali CEM III/B–
829 SiO₂ cement (LAC). *Cem. Concr. Res.* 42, 410–423.
830 <https://doi.org/10.1016/J.CEMCONRES.2011.11.008>
- 831 Lothenbach, B., Wieland, E., Schwyn, B., Figi, R., Rentsch, D., 2008. Hydration of low-pH cements., in:
832 *International Workshop on the Mechanisms and Modelling of Cement / Waste Interactions., Le*
833 *Croisic, France,*
- 834 Mäder, U., Jenni, A., Lerouge C., Gaboreau, S., Miyoshi, S., Kimura, Y, Cloet, V., Fukaya, M., Claret, F., Otake,
835 T, Shibata M., Lothenbach B. (2017). 5-year chemico-physical evolution of concrete–claystone
836 interfaces, Mont Terri rock laboratory (Switzerland). *Swiss J. Geosci.* 110, 307.
- 837 Mancini, A., Wieland, E., Geng, G., Dähn, R., Skibsted, J., Wehrli, B. Lothenbach B (2020) Fe (III) uptake by
838 calcium silicate hydrates. *Applied Geochemistry*, 113, 104460

- 839 Martino, J.B., 2007. Low heat high performance concrete used in a full-scale tunnel seal, in: Proceeding 3rd
840 Workshop R&D on Low PH Cement for a Geological Repository, Paris, June. pp. 13–14.
- 841 Moren, L., 2010. Design and production of the KBS-3 repository, Technical. Report TR-10-12 ed. Svenskt
842 Kärnbränslehantering AB.
- 843 Nagra, 2019 n.d. Timetable [WWW Document]. Nagra. URL <https://www.nagra.ch/en/timetable.htm#>
844 (accessed 6.28.19).
- 845 Nikitenko, S., Beale, A.M., van der Eerden, A.M.J., Jacques, S.D.M., Leynaud, O., O'Brien, M.G.,
846 Detollenaere, D., Kaptein, R., Weckhuysen, B.M., Bras, W., 2008. Implementation of a combined
847 SAXS/WAXS/QEXAFS set-up for time-resolved {in situ} experiments. *J. Synchrotron Radiat.* 15, 632–
848 640. <https://doi.org/10.1107/S0909049508023327>
- 849 Nishiuchi, T., Yamamoto, T., Hironaga, M., Ueda, H., 2007. Mechanical properties of low pH concretes, LAC,
850 HFSC AND SAC, in: Proceeding 3rd Workshop R&D on Low PH Cement for a Geological Repository,
851 Paris, June. pp. 13–14.
- 852 Noiret, A., Bethmont, S., Bosgiraud, J., Foin, R., 2012. DOPAS Work Package 4 Deliverable 4.8FSS
853 Experiment Summary Report.
- 854 Palomäki, J., Ristimäki, L., 2013. Facility Description 2012: Summary Report of the Encapsulation Plant and
855 Disposal Facility Designs, Working Report 2012-66.
- 856 Posiva Oy, 2020 n.d. General Time Schedule for Final Disposal [WWW Document]. Posiva Oy Olkiluoto,
857 27160 Eurajoki.
858 http://www.posiva.fi/en/final_disposal/general_time_schedule_for_final_disposal#.XorbmEASs2w.
859 (accessed 06.04.20).
- 860 Proux, O., Nassif, V., Prat, A., Ulrich, O., Lahera, E., Biquard, X., Menthonnex, J.-J., Hazemann, J.-L., 2006.
861 Feedback system of a liquid-nitrogen-cooled double-crystal monochromator: design and
862 performances. *J. Synchrotron Radiat.* 13, 59–68. <https://doi.org/10.1107/S0909049505037441>
- 863 Ravel, B., Newville, M., 2005. Data analysis for X-ray absorption spectroscopy using IFEFFIT. *J. Synchrotron
864 Radiat.* 12, 537–541. <https://doi.org/10.1107/S0909049505012719>
- 865 Richardson, I., 1999. The nature of C-S-H in hardened cements. *Cem. Concr. Res.* 29, 1131–1147.
866 [https://doi.org/10.1016/S0008-8846\(99\)00168-4](https://doi.org/10.1016/S0008-8846(99)00168-4)
- 867 Rothe, J., Butorin, S., Dardenne, K., Denecke, M.A., Kienzler, B., Löble, M., Metz, V., Seibert, A., Steppert,
868 M., Vitova, T., Walther, C., Geckeis, H., 2012. The INE-Beamline for actinide science at ANKA. *Rev. Sci.
869 Instrum.* 83, 043105. <https://doi.org/10.1063/1.3700813>
- 870 Roos, C. 2016. Thermodynamic properties of hydrated cement phases: C-S-H, C-A-S-H and M-S-H. Thesis,
871 Université de Poitiers, France
- 872 Roos, C., Grangeon, S., Blanc, P., Montouillout, V., Lothenbach, B., Henocq, P., Giffaut E., Vieillard, P.,
873 Gaboreau, S. 2015 Crystal structure of magnesium silicate hydrates (MSH): The relation with 2: 1 Mg-
874 Si phyllosilicates. *Cement and Concrete Research* 73, 228-237
- 875 Roos, C., Vieillard, P., Blan, P., Gaboreau, S., Gailhanou, H., Braithwaite, D., Montouillout, V., Denoyel, R.,
876 Henocq, P., Madé, B. Thermodynamic properties of C-S-H, C-A-S-H and M-S-H phases. 2018. Results
877 from direct measurements and predictive modelling. *Applied Geochemistry*, 92, 140-156
- 878 Schöler, A., Lothenbach, B., Winnefeld, F., Zajac, M., 2015. Hydration of quaternary Portland cement blends
879 containing blast-furnace slag, siliceous fly ash and limestone powder. *Cement Concrete Composite* 55,
880 374–382.

- 881 Scrivener, K., Snellings, R., Lothenbach, B., 2018. A practical guide to microstructural analysis of
882 cementitious materials. Crc Press. Taylor and Francis Group
- 883 Taylor, H.F.W., 1997. Cement Chemistry, 2nd ed. Thomas Telford Publishing, Thomas Telford Services Ltd,
884 London.
- 885 Turrero, M., Fernández, A., Peña, F., SÁNCHEZ, M.D., Wersin, P., Bossart, P., Sánchez, M., MELÓN, A.,
886 Garralón, A., de Llano, A., Gómez, P., HERNÁN, P., 2006. Pore water chemistry of a Paleogene
887 continental mudrock in Spain and a Jurassic marine mudrock in Switzerland: Sampling methods and
888 geochemical interpretation. *J. Iber. Geol.* 2006.
- 889 Turrero, M., Villar, M., Torres, E., Escribano, A., Cuevas, J., Fernandez, R., Ruiz, A., Vigil de la Villa, R., Soto,
890 I., 2011. Laboratory tests at the interfaces: first results on dismantling of tests FB3 and HB4. PEBS Proj.
891 Deliv. D2.3-3-1.
- 892 Vasconcelos, R. Walkley, B., Day, S. Tang C., Paraskevoulakos H., Gardner L, Corkhill C. (2020) 18-month
893 hydration of a low-pH cement for geological disposal of radioactive waste: The Cebama reference
894 cement, *Applied Geochemistry*, in print
- 895 Vašíček, R., Červinka, R., P, V., T, R., J, S., 2018. Geochemical and Thermal Impacts on the Characteristics of
896 Cementitious Materials: Strength, Leachate pH, Mineralogy And Diffusion, in: Third Annual Workshop
897 of the HORIZON 2020 CEBAMA Project. Nantes.
- 898 Vašíček, R., Večerník, P., Hloušek, J., Červinka, R., Hausmannová, L., Havlová, V., 2019. Interaction between
899 cement and Czech bentonite under temperature load and in in-situ conditions: results after first
900 testing period, in Altmaier et al. : Proceedings of the Second Workshop of the HORIZON 2020 CEBAMA
901 Project. KIT Scientific Reports; 7752. p. 93.
- 902 Večerník, P., Hausmannová, L., Cervinka, R., Vašíček, R., Roll, M., Hloušek, J., Havlová, V., 2016. Interaction
903 between cement and Czech bentonite under temperature load and in in-situ conditions: an overview
904 of experimental program. In Altmaier et al. 1st Annual workshop cebama proceedings cebama Proc.
905 KIT Scientific report 7734, 77, Germany.
- 906 Vehmas, T., Schnidler, A., Löjja, M., Leivo, M., Holt, E., 2017. Reference mix design and castings for low-pH
907 concrete for nuclear waste repositories. *Horiz. 2020 CEBAMA Proj.* 101.
- 908 Vespa M., E. Wieland, R. Dähn, B. Lothenbach (2015) Identification of the thermodynamically stable Fe-
909 containing phase in aged cement pastes. *J. Am. Ceram. Soc.* 98, 2286
- 910 Vinsot, A., Mettler, S., Wechner, S., 2008. In situ characterization of the Callovo-Oxfordian pore water
911 composition. *Phys. Chem. Earth, Parts A/B/C* 33, S75–S86. <https://doi.org/10.1016/J.PCE.2008.10.048>
- 912 Walkley B, Provis J.L. 2019 Solid-state nuclear magnetic resonance spectroscopy of cements. *Materials*
913 *Today Advances*, 1, 100007
- 914 Washburn, E.W., 1921. The dynamics of capillary flow. *Phys. Rev.* 17, 273.
- 915 Westre, T.E., Kennepohl, P., DeWitt, J.G., Hedman, B., Hodgson, K.O., Solomon, E.I., 1997. A Multiplet
916 Analysis of Fe K-Edge 1s → 3d Pre-Edge Features of Iron Complexes. *J. Am. Chem. Soc.* 119, 6297–
917 6314. <https://doi.org/10.1021/ja964352a>
- 918 World Nuclear Association, n.d. Radioactive waste Management [WWW Document]. URL
919 [http://www.world-nuclear.org/information-library/nuclear-fuel-cycle/nuclear-wastes/radioactive-](http://www.world-nuclear.org/information-library/nuclear-fuel-cycle/nuclear-wastes/radioactive-waste-management.aspx)
920 [waste-management.aspx](http://www.world-nuclear.org/information-library/nuclear-fuel-cycle/nuclear-wastes/radioactive-waste-management.aspx) (accessed 28.06.19).
- 921 Zhang, Z., Zhu, Y., Zhu, H., Zhang, Y., Provis, J.L., Wang, H., 2019. Effect of drying procedures on pore
922 structure and phase evolution of alkali-activated cements. *Cem. Concr. Compos.* 96, 194–203.
923 <https://doi.org/10.1016/J.CEMCONCOMP.2018.12.003>

